

# CHIPS: Efficient CLIP Adaptation via Curvature-aware Hybrid Influence-based Data Selection

Xinlin Zhuang<sup>1,2,5</sup> Yichen Li<sup>1,3</sup> Xiwei Liu<sup>1</sup> Haolin Yang<sup>1</sup> Yifan Lu<sup>1</sup>  
Ziyun Zou<sup>1</sup> Yulong Li<sup>1</sup> Huifa Li<sup>1</sup> Dongliang Chen<sup>2</sup> Qinglei Wang<sup>1</sup>  
Weiyang Liu<sup>5</sup> Ying Qian<sup>2\*</sup> Jiangming Shi<sup>4\*</sup> Imran Razzak<sup>1\*</sup>

<sup>1</sup>MBZUAI <sup>2</sup>East China Normal University <sup>3</sup>Huazhong University of Science and Technology  
<sup>4</sup>Xiamen University <sup>5</sup>The Chinese University of Hong Kong

xinlinzhuang@stu.ecnu.edu.cn, yqian@cs.ecnu.edu.cn, jiangming.shi@outlook.com, imran.razzak@mbzuai.ac.ae

## Abstract

Adapting CLIP to vertical domains is typically approached by novel fine-tuning strategies or by continual pre-training (CPT) on large domain-specific datasets. Yet, data itself remains an underexplored factor in this process. We revisit this task from a data-centric perspective: Can effective data selection substitute for large-scale datasets in CPT? We introduce **CHIPS** (Curvature-aware Hybrid Influence in Projection Subspace), which assigns each image-text pair a utility score that integrates three complementary factors aligned with three goals: faithfulness via a curvature-aware, Newton-style alignment computed in CLIP’s endpoint subspace; scalability via an InfoNCE-aware curvature estimator with Johnson-Lindenstrauss (JL) sketching; and retention via a selection-aware relevance weight combined with learnability to balance target adaptation against general-domain preservation. We justify this design theoretically by proving a lower-bound guarantee on the proxy’s correlation with full-parameter alignment and by characterizing the bias-variance trade-offs introduced by curvature mixing and JL sketching. We evaluate CHIPS empirically across various settings: 1) CHIPS attains state-of-the-art performance among selection baselines on 17 **medical benchmarks**, matches full-dataset CPT with 30% of the data, and outperforms half-dataset CPT using only 10%; 2) on 31 **general-domain benchmarks**, CHIPS yields the smallest performance drop under 10–30% data-retention budgets. Code, data, and checkpoints will be released.

## 1. Introduction

Vision-language models such as CLIP [44] achieve strong zero-shot recognition in general domains, but their perfor-

Method	Target	Sketch	Curvature	Domain	CLIP
Full CPT	✗	✗	✗	✗	✗
Random Selection	✗	✗	✗	✗	✗
Rule-filter	✗	✗	✗	✗	✗
CLIPscore	✗	✗	✗	✗	✗
Dot	✓	✓	✗	✗	✗
TracIn	✓	✓	✗	✗	✗
TRAK	✓	✓	✓	✗	✗
<b>CHIPS (ours)</b>	✓	✓	✓	✓	✓

Table 1. Properties of data selection methods for CLIP adaptation. *Target*: whether the strategy utilizes target evaluation set information. *Sketch*: whether JL Sketch is supported. *Curvature*: whether second-order information is employed. *Domain*: whether general-target domain balance is supported. *CLIP*: whether the method is specifically designed for CLIP models.

mance degrades sharply in vertical settings (e.g., medical imaging and biology) where vocabulary, acquisition protocols, and label taxonomies shift substantially [66]. To adapt CLIP to such domains, two main paradigms have emerged: 1) *Model-centric* methods modify training or parameterization (e.g., probabilistic fine-tuning [25], many-to-many contrastive learning [24], and PEFT variants [18, 35, 46, 58, 65]); 2) *Data-centric* methods pursue continual pre-training (CPT) on large, domain-specific datasets, ranging from millions to hundreds of millions of pairs across medical and biodiversity settings [4, 15, 17, 23, 34, 36, 48, 50, 54, 59, 60, 64]. However, for vertical domains, collecting, curating, and processing ever-larger datasets is costly, and indiscriminate upsampling can even dilute learning with redundant, low-utility samples. This naturally raises a question: *Is sheer scale truly necessary for effective CPT?*

Meanwhile, a complementary line of work studies data attribution [9] to quantify how individual samples affect training dynamics and downstream generalization. Classical influence functions [28] and variants such as

\*Corresponding authors.

TracIn [43], EL2N [42], Arnoldi/GEX/FVM [27, 47, 62], were developed for single-tower model on supervised classification with additive cross-entropy and full-parameter updates. In CLIP, three mechanisms break these assumptions and systematically mis-rank examples. **(A) Cross-modal curvature of dual encoders.** CLIP’s dual encoders induce non-block-diagonal second-order curvature and block-diagonal proxies ignore this coupling and mis-rank samples. **(B) Non-local gradients under InfoNCE.** Each sample’s gradient depends on the softmax normalizer over the full negative set, making influence *batch-/global-dependent* rather than per-example additive and thus sensitive to batch size, queue design, and negative composition. **(C) End-point dominance at the projection heads.** Empirically, the projection heads and temperature drive early shifts in similarity distributions, whereas backbone updates are smaller and slower, rendering full-parameter updates partially unnecessary at the early stage.

Motivated by (A)–(C), we propose **CHIPS** (Curvature-aware Hybrid Influence in Projection Subspace), a CLIP-specific selector that scores each candidate by the expected one-step drop of the target evaluation loss and selects the top examples for CPT. CHIPS is designed for three goals, *faithfulness*, *scalability*, and *retention*, with one component per goal: (i) a Newton-style alignment computed on the projection heads and temperature that *provably lower-bounds* full-parameter alignment and enjoys better conditioning (Sec. 2.2); (ii) an InfoNCE-aware curvature preconditioner built from positive/negative gradient moments and compressed via Johnson–Lindenstrauss (JL) sketch to achieve near-linear time/memory with a quantified variance–bias trade-off (Sec. 2.3); and (iii) a selection-aware *soft* weighting that combines per-sample learnability with target-domain relevance to explicitly control the adaptation–retention balance (Sec. 2.4). Tab. 1 summarizes the dimensions that matter in practice and positions CHIPS against several common baselines.

Across **17** medical benchmarks, CHIPS *matches* full-dataset CPT using only **30%** of the training pool, and *outperforms* half-dataset CPT using merely **10%** data, achieving state-of-the-art among selection baselines. For **31** general-domain benchmarks, although domain adaptation inevitably reduces average performance, CHIPS consistently *reduces* the drop relative to the previous SOTA selector, indicating stronger retention of general-domain capabilities. In short, with principled attribution and CLIP-aware curvature, *effective CPT does not require extreme scale*.

Our contributions are threefold:

- **Curvature-aware proxy alignment in CLIP’s end-point subspace.** We define a Newton-inspired alignment that ranks samples by expected one-step decrease on the target validation loss and provably lower-bounds full-parameter alignment.

- **InfoNCE-aware curvature estimation with JL sketching and guarantees.** We incorporate negative-pair geometry to capture cross-example curvature and characterize the variance–bias trade-off of the estimator.
- **Selection-aware weighting for learnability and retention.** We combine learnability and domain-relevance weights to emphasize decision-boundary, on-domain samples while softly limiting selection drift, mitigating catastrophic forgetting of general-domain knowledge.

## 2. Method

CHIPS ranks training samples for CPT by estimating, for each sample, how much a one-step update would decrease the evaluation loss on the target domain. We operationalize this idea along three tightly coupled components: (i) a curvature-aware proxy alignment score computed in CLIP’s end-point geometry (projection heads and temperature), (ii) a negative-pair curvature estimator that captures the second-order coupling induced by symmetric InfoNCE and scales via JL sketching, and (iii) two multiplicative weights for learnability and target-domain relevance, forming a single selection utility. Fig. 1 provides the workflow of CHIPS.

### 2.1. Problem Setup

We consider a pre-trained general CLIP model with parameters  $\theta$  and a large target-domain training pool  $\mathcal{D}_{\text{pool}} = \{z_i\}_{i=1}^N$  of image–text pairs. Our goal is to select a valuable subset from  $\mathcal{D}_{\text{pool}}$  for CPT so as to maximize performance on a held-out target-domain evaluation set  $\mathcal{D}_{\text{eval}}$  consisting of samples from various validation sets of downstream tasks. Let  $\mathcal{L}_{\text{eval}}(\theta) \triangleq \mathbb{E}_{z \sim \mathcal{D}_{\text{eval}}}[\ell(z; \theta)]$  denote the evaluation loss, where  $\ell$  is the symmetric InfoNCE objective [44] with a learnable logit-scale (temperature)  $\tau > 0$ . Denote the evaluation mean gradient by  $\mathbf{u} \triangleq \nabla_{\theta} \mathcal{L}_{\text{eval}}(\theta) = \mathbb{E}_{z \sim \mathcal{D}_{\text{eval}}}[\nabla_{\theta} \ell(z; \theta)]$ . During CPT, one Stochastic Gradient Descent (SGD) step draws a mini-batch of size  $B$  from a selection distribution  $q$  and computes the batch gradient  $\hat{\mathbf{g}} = \frac{1}{B} \sum_{i=1}^B \nabla_{\theta} \ell(z_i; \theta)$  to update parameters via

$$\theta' = \theta - \eta \hat{\mathbf{g}}, \quad (1)$$

where  $\eta > 0$  is the learning rate. We also define the training mean gradient under  $q$  by  $\mathbf{g}_q \triangleq \mathbb{E}_{z \sim q}[\nabla_{\theta} \ell(z; \theta)]$ . Assume  $\mathcal{L}_{\text{eval}}$  is twice continuously differentiable in a neighborhood of  $\theta$  and let  $\mathbf{H}_{\text{eval}}(\theta) = \nabla_{\theta}^2 \mathcal{L}_{\text{eval}}(\theta)$ . A second-order Taylor expansion with integral remainder and Hessian-Lipschitz constant  $L_H$  yields, for  $\Delta\theta = -\eta \hat{\mathbf{g}}$ ,

$$\mathbb{E}[\Delta \mathcal{L}_{\text{eval}}] \leq -\eta \mathbf{g}_q^{\top} \mathbf{u} + \frac{1}{2} \eta^2 \mathbb{E}[\hat{\mathbf{g}}^{\top} \mathbf{H}_{\text{eval}}(\Theta) \hat{\mathbf{g}}] + \frac{L_H}{6} \eta^3 \mathbb{E}[\|\hat{\mathbf{g}}\|^3], \quad (2)$$

for some  $\Theta$  on the segment between  $\theta$  and  $\theta'$ . In a local quadratic model, the steepest descent direction is the

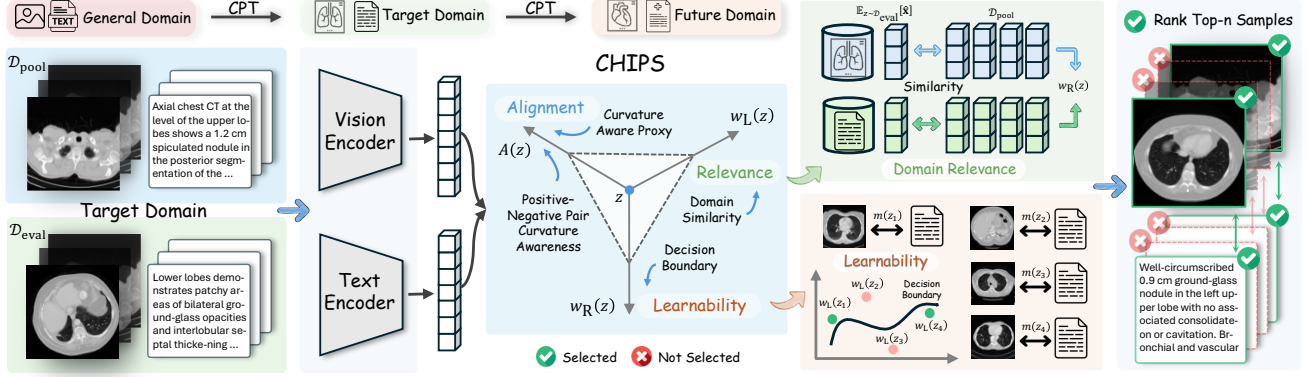


Figure 1. Workflow of CHIPS. For each training sample, CHIPS computes a curvature-aware proxy Newton alignment in CLIP’s end-point space (projection heads and temperature), where curvature is approximated by mixing self and negative-pair cross moments from symmetric InfoNCE and scaled efficiently via JL sketching. The alignment is then modulated by learnability and target-domain relevance to yield a single selection utility, and the top- $n$  samples are chosen to CPT CLIP models for domain adaptation.

Newton direction  $\mathbf{H}_{\text{eval}}^{-1} \mathbf{u}$ , and a good selection distribution  $q$  should **increase** the first-order alignment term  $-\eta \mathbf{g}_q^\top \mathbf{u}$  while controlling curvature. For a more lightweight assumption, if  $\mathcal{L}_{\text{eval}}$  is  $\rho$ -smooth (gradient-Lipschitz), then

$$\mathbb{E}[\Delta \mathcal{L}_{\text{eval}}] \leq -\eta \mathbf{g}_q^\top \mathbf{u} + \frac{\rho}{2} \eta^2 \mathbb{E}[\|\hat{\mathbf{g}}\|^2]. \quad (3)$$

Eq. (2) and Eq. (3) emphasize the same principle: *descent is driven by the alignment between the expected training gradient and the evaluation mean gradient*. While we present SGD for clarity, the alignment direction naturally extends to AdamW and full proofs are provided in App. B.1. These observations motivate us to prioritize samples whose updates align with (a proxy of) the Newton direction; the construction of such a curvature-aware proxy in CLIP’s end-point geometry is given next in Sec. 2.2.

## 2.2. Curvature-aware Proxy Alignment

Given CLIP’s dual-encoder with projection heads and a temperature, we implement CHIPS in the end-point subspace consisting of projection heads and temperature  $\vartheta = \{\mathbf{W}_v, \mathbf{W}_t, \tau\}$ . For a sample  $z$ , let  $\mathbf{g}_\vartheta(z) = \nabla_\vartheta \ell(z; \theta)$  be its gradient restricted to  $\vartheta$ , and define the evaluation mean  $\mathbf{u}_\vartheta = \mathbb{E}_{z \sim \mathcal{D}_{\text{eval}}}[\mathbf{g}_\vartheta(z)]$ . For reference, denote the full-parameter gradient by  $\mathbf{g}_\theta(z) = \nabla_\theta \ell(z; \theta)$  and its evaluation mean by  $\mathbf{u} = \mathbb{E}_{z \sim \mathcal{D}_{\text{eval}}}[\mathbf{g}_\theta(z)]$ . Motivated by the one-step descent view in Sec. 2.1, an ideal update direction on  $\vartheta$  is the Newton direction  $\mathbf{H}_\vartheta^{-1} \mathbf{u}_\vartheta$ , where  $\mathbf{H}_\vartheta$  denotes a population curvature (e.g., generalized Gauss–Newton) on the subspace. We therefore define a curvature-aware proxy Newton alignment for each sample:

$$A(z) \triangleq \mathbf{g}_\vartheta(z)^\top \mathbf{M}^{-1} \mathbf{u}_\vartheta, \quad (4)$$

where  $\mathbf{M} \succ 0$  is a tractable curvature surrogate instantiated in Sec. 2.3. The sign and magnitude of  $A(z)$  indicate

whether (and how strongly) a one-step update on  $z$  moves the model along a descent direction for the evaluation loss: **large positive**  $A(z)$  is preferred.

Directly computing alignment with respect to all parameters is expensive and brittle to high-dimensional noise. We instead argue that the end-point geometry is a reliable proxy for full alignment. Eq. (4) can be rewritten as  $A(z) = \tilde{\mathbf{g}}_\vartheta(z)^\top \tilde{\mathbf{u}}_\vartheta$  with  $\tilde{\mathbf{g}}_\vartheta = \mathbf{M}^{-1/2} \mathbf{g}_\vartheta$  and  $\tilde{\mathbf{u}}_\vartheta = \mathbf{M}^{-1/2} \mathbf{u}_\vartheta$ . Thus  $\mathbf{M}$  is a fixed (sample-independent) preconditioner and the proxy–full correlation bound applies unchanged after the congruent transform, i.e., replace  $\Sigma_g$  by  $\mathbf{M}^{-1/2} \Sigma_g \mathbf{M}^{-1/2}$  and  $\mathbf{S}$  by  $\mathbf{M}^{1/2} \mathbf{S} \mathbf{M}^{1/2}$ . We can state a single unified bound below.

Consider the following local linearization:

$$\nabla_\theta \ell(z) = \mathbf{J} \mathbf{g}_\vartheta(z) + \mathbf{r}(z), \quad \mathbf{u} = \bar{\mathbf{J}} \mathbf{u}_\vartheta + \boldsymbol{\varepsilon}, \quad (5)$$

and define  $X(z) = \mathbf{g}_\vartheta(z)^\top \mathbf{u}_\vartheta$ ,  $Y(z) = \mathbf{g}_\theta(z)^\top \mathbf{u}$  with Pearson correlation  $\rho_{XY}$ ,  $\Sigma_g = \text{Cov}[\mathbf{g}_\vartheta(z)]$ ,  $\mathbf{S} = \frac{1}{2}(\mathbf{J}^\top \bar{\mathbf{J}} + \bar{\mathbf{J}}^\top \mathbf{J})$ ,  $\mathbf{B} = \Sigma_g^{1/2} \mathbf{S} \Sigma_g^{-1/2}$ , and  $\sigma_\zeta^2 = \text{Var}[\zeta(z)]$  for the mismatch term induced by  $(\mathbf{r}, \boldsymbol{\varepsilon})$ .

**Theorem 1** (Proxy–full alignment correlation). *If  $\zeta(z)$  is uncorrelated with  $\mathbf{g}_\vartheta(z)$ , then*

$$\rho_{XY} \geq \frac{\lambda_{\min}(\text{sym}(\mathbf{B}))}{\sqrt{\|\mathbf{B}\|_2^2 + \sigma_\zeta^2 / (\mathbf{u}_\vartheta^\top \Sigma_g \mathbf{u}_\vartheta)}}. \quad (6)$$

The matrices  $\mathbf{S}$  and  $\Sigma_g$  summarize how end-point gradients relate to full-parameter gradients and how they vary. When  $\mathbf{S}$  is well-conditioned along  $\text{span}(\mathbf{u}_\vartheta)$  and the mismatch variance  $\sigma_\zeta^2$  is modest, the bound keeps  $\rho_{XY}$  bounded away from zero, so ranking by the proxy alignment tracks the full alignment. Under approximate isotropy

or commuting structure, the expression simplifies by effectively replacing  $\mathbf{B}$  with  $\mathbf{S}$  (see App. B.2). Empirically, on a 100K subset of BIOMEDICA [36], Spearman’s  $\rho_s = 0.83$  between proxy and full alignment supports this proxy view.

### 2.3. Curvature Estimation

Symmetric InfoNCE couples each positive pair with many negatives through the softmax normalizer, creating *cross-example* curvature that a positive-only or diagonal surrogate fails to capture. Since our alignment score  $A(z)$  relies on a curvature-preconditioned inner product, missing this cross mass yields a biased Newton proxy and unstable rankings along highly coupled directions. Working in the end-point subspace  $\vartheta$ , we approximate the population curvature (e.g., generalized Gauss–Newton) by combining self and cross second moments of subspace gradients:

$$\begin{aligned}\Phi_{\text{pos}} &= \frac{1}{N} \sum_{i=1}^N \mathbf{g}_{\vartheta}(z_i) \mathbf{g}_{\vartheta}(z_i)^{\top}, \\ \Phi_{\text{neg}} &= \frac{1}{N(N-1)} \sum_{i \neq j} \mathbf{g}_{\vartheta}(z_i) \mathbf{g}_{\vartheta}(z_j)^{\top},\end{aligned}\tag{7}$$

where  $\Phi_{\text{pos}}$  captures *self* curvature, while  $\Phi_{\text{neg}}$  restores the *cross* mass induced by random negatives in InfoNCE. We then form a trace- and spectrum-controlled surrogate

$$\mathbf{H}_{\vartheta}^{(\alpha)} = (1 - \alpha) \Phi_{\text{pos}} + \alpha \Phi_{\text{neg}}, \quad \mathbf{M} = \mathbf{H}_{\vartheta}^{(\alpha)} + \lambda \mathbf{I}, \tag{8}$$

with a mixing weight  $\alpha \in [0, 1]$  and a small Tikhonov parameter  $\lambda > 0$  to ensure numerical stability in matrix inversion. Plugging  $\mathbf{M}$  into Eq. (4) yields the *curvature-aware* proxy Newton score  $A(z)$ . By mixing  $\Phi_{\text{pos}}$  with the cross moment  $\Phi_{\text{neg}}$  (with  $\alpha > 0$ ), we restore the off-diagonal curvature induced by InfoNCE’s negatives that positive-only surrogates ignore. The surrogate  $\mathbf{M} \succ 0$  thus preconditions  $A(z)$  in a fixed metric without altering the proxy–full correlation framework (Sec. 2.2);  $\alpha$  controls coupling strength and  $\lambda$  provides ridge stability. This yields an alignment score that is sensitive to the true second-order structure yet robust. Let the ideal scalar be  $A^*(z) = \mathbf{g}_{\vartheta}(z)^{\top} \mathbf{H}_{\vartheta}^{-1} \mathbf{u}_{\vartheta}$  and the curvature-approximated score  $A_{\alpha}(z) = \mathbf{g}_{\vartheta}(z)^{\top} \mathbf{M}^{-1} \mathbf{u}_{\vartheta}$  with  $\mathbf{M}$  as in Eq. (8), and define  $\Delta_{\alpha} = \mathbf{H}_{\vartheta} - \mathbf{H}_{\vartheta}^{(\alpha)}$ . For further efficiency, we apply a  $k$ -dimensional JL sketch to compute a sketched score  $\hat{A}_{\alpha}(z)$ . We discuss the choice of JL sketch in Sec. 4.1.

**Theorem 2** (Error bound for curvature mixing). *Assume bounded spectra for  $\mathbf{H}_{\vartheta}$  and  $\mathbf{H}_{\vartheta}^{(\alpha)}$ . Then, with probability at least  $1 - \delta$  over the JL sketch (vacuous if no sketch is used), there exist constants  $C_1, C_2 > 0$ , depending only on*

*spectral bounds of  $\mathbf{H}_{\vartheta}$  and  $\mathbf{H}_{\vartheta}^{(\alpha)}$ , such that*

$$\begin{aligned}\mathbb{E}_z[(\hat{A}_{\alpha}(z) - A^*(z))^2] &\leq \underbrace{\frac{C_1 \log(1/\delta)}{k}}_{\text{projection variance}} \\ &\quad + \underbrace{C_2 \|\Delta_{\alpha}\|_F^2 \|\mathbf{H}_{\vartheta}^{-1} \mathbf{u}_{\vartheta}\|_2^2}_{\text{curvature bias}}.\end{aligned}\tag{9}$$

Eq. (9) separates an  $O(1/k)$  *projection variance* term and a *curvature bias* term that shrinks as  $\mathbf{H}_{\vartheta}^{(\alpha)}$  better matches  $\mathbf{H}_{\vartheta}$ . Because  $\Phi_{\text{neg}}$  restores off-diagonal mass whenever cross-example coupling is present, any  $\alpha > 0$  that does so reduces  $\|\Delta_{\alpha}\|_F$  and tightens the bound;  $\lambda$  stabilizes the inverse without changing the decomposition. All derivations and proofs are deferred to App. B.3.

### 2.4. Learnability and Domain Relevance

The curvature-aware alignment score  $A(z)$  in Eq. (4) indicates whether a sample points in a *useful* descent direction, but it does not distinguish already-solved cases from borderline ones, nor does it compensate for the distributional gap between  $\mathcal{D}_{\text{pool}}$  and  $\mathcal{D}_{\text{eval}}$ . Therefore, we introduce another two multiplicative weights to modulate  $A(z)$  by *learnability* and *target-domain relevance*.

**Learnability.** For a mini-batch of paired image–text examples  $\{(x_i, y_i)\}_{i=1}^B$ , let the end-point embeddings be  $\hat{\mathbf{x}}_i = \frac{\mathbf{W}_v \mathbf{h}_i}{\|\mathbf{W}_v \mathbf{h}_i\|}$  and  $\hat{\mathbf{y}}_j = \frac{\mathbf{W}_t \mathbf{t}_j}{\|\mathbf{W}_t \mathbf{t}_j\|}$  with temperature  $\tau > 0$ . The CLIP similarity is  $s_{ij} = \tau \hat{\mathbf{x}}_i^{\top} \hat{\mathbf{y}}_j$ , with softmax probabilities  $p_{ij}^{2t} = \frac{\exp(s_{ij})}{\sum_{j'} \exp(s_{ij'})}$  and  $p_{ij}^{2i} = \frac{\exp(s_{ij})}{\sum_{i'} \exp(s_{i'j})}$ . Define the average correctness and a hardest-negative margin as

$$\begin{aligned}p_{\text{corr}}(z) &= \frac{1}{2} (p_{ii}^{2t} + p_{ii}^{2i}), \\ m(z) &= s_{ii} - \max\left\{ \max_{j \neq i} s_{ij}, \max_{i' \neq i} s_{i'i} \right\}.\end{aligned}\tag{10}$$

We then weight toward decision-boundary examples and away from saturated ones:

$$w_L(z) = (1 - p_{\text{corr}}(z)) (1 + \sigma(-m(z))), \tag{11}$$

where  $\sigma(\cdot)$  is the sigmoid function. The first factor down-weights already-correct and high-confidence pairs to reduce their impact while the second emphasizes small/negative margins that are most learnable in one step.

**Target-domain Relevance.** To softly favor samples consistent with  $\mathcal{D}_{\text{eval}}$ , we compute evaluation embeddings  $\boldsymbol{\mu}_x = \mathbb{E}_{z \sim \mathcal{D}_{\text{eval}}}[\hat{\mathbf{x}}]$ ,  $\boldsymbol{\mu}_y = \mathbb{E}_{z \sim \mathcal{D}_{\text{eval}}}[\hat{\mathbf{y}}]$ , and define

$$w_R(z) = \sigma\left((1 - \beta) \cos(\hat{\mathbf{x}}, \boldsymbol{\mu}_x) + \beta \cos(\hat{\mathbf{y}}, \boldsymbol{\mu}_y)\right), \tag{12}$$

where  $\beta \in [0, 1]$  controls the balance between two modalities and  $\cos(\cdot, \cdot)$  denotes the cosine similarity. Notably, the

relevance logit  $s(z) = (1-\beta) \cos(\hat{\mathbf{x}}, \boldsymbol{\mu}_x) + \beta \cos(\hat{\mathbf{y}}, \boldsymbol{\mu}_y)$  in Eq. (12) lies in  $[-1, 1]$ , therefore  $w_R(z) \in [\sigma(-1), \sigma(1)] \approx [0.27, 0.73]$ . This implements soft re-weighting to some extent rather than hard filtering as no sample is zeroed out.

Let  $\tilde{q} \propto A(\cdot) w_L(\cdot)$  and  $q \propto w_R(\cdot) \tilde{q}$  be the selection distributions with/without  $w_R$ . Because  $w_R \in [a, b]$  with  $a = \sigma(-1)$ ,  $b = \sigma(1)$ , the density ratio  $r(z) = \frac{q(z)}{\tilde{q}(z)} = \frac{w_R(z)}{\mathbb{E}_{\tilde{q}}[w_R]}$  satisfies  $r(z) \in [a/b, b/a] = [e^{-1}, e]$ , which implies a bounded selection drift  $D_{\text{KL}}(q \parallel \tilde{q}) \leq 1$  nat. Thus  $w_R$  also *limits* how far the selection moves from the base alignment-driven distribution, mitigating catastrophic forgetting of general-domain knowledge. We analyze  $\beta$  in Sec. 4.2 to balance adaptation and retention.

**Final utility score and selection.** We combine the components multiplicatively into a single ranking score.

$$\mathcal{I}_{\text{CHIPS}}(z) = \hat{A}_\alpha(z) \cdot w_L(z) \cdot w_R(z), \quad (13)$$

and select the top- $n$  examples from  $\mathcal{D}_{\text{pool}}$  for CPT. Implementation details of CHIPS are provided in App. C.

## 3. Experiment

### 3.1. Experimental Setup

**Training.** For a comprehensive comparison, we perform continual pre-training using the initialization weights of MetaCLIP-B32/B16/L14/H14 [57]. We select **medical** as target domain and two recently introduced large-scale medical multimodal datasets are employed as training pools: BIOMEDICA (24M samples) [36] and MedTrinity (18M samples) [56]. We select data retention ratio  $r$  as 10%, 20%, 30%, and 50% of the complete dataset, with the number of training epochs fixed at 5. All models are optimized using the AdamW optimizer ( $\beta_1 = 0.9, \beta_2 = 0.98, \epsilon = 10^{-6}$ ) and a cosine learning rate scheduler (initial learning rate as  $10^{-6}$ ), with a global batch size of 32,768. Each experiment is conducted on an Ubuntu 24.04 server equipped with 8x NVIDIA H200 (141GB) GPUs. Further details regarding the training datasets, model architectures, and specific hyperparameter settings are provided in App. E.

**Evaluation.** We evaluate 48 tasks spanning general and medical domains to enable a comprehensive assessment. The general-domain suite includes Cars [29], Country211 [44], Fer2013 [16], Aircraft [37], Food101 [3], GTSRB [49], ImageNet-A, ImageNet-O [20], ImageNet-1K [8], ImageNetV2 [45], MNIST [31], Rendered-SST2 [44], STL-10 [7], SUN397 [55], VOC [12], Caltech-101 [13], CIFAR-10, CIFAR-100 [30], CLEVR (Closest-Object-Distance/Count-All) [26], DTD [6], EuroSAT [19], Oxford Flowers [39], KITTI [14], Pets [41], RESISC45 [5], smallNORB (Azimuth), smallNORB (Elevation) [32], SVHN [38], Flickr8k

[22], Flickr30k [63], and MSCOCO [33]. For the medical domain, we consider 17 classification tasks across eight specialties. These include Ophthalmology (Diabetic [11], OCTMNIST, RetinaMNIST [61]); Radiology (ChestMNIST, ChestX-ray14 [52], OrganAMNIST, OrganCMNIST, OrganSMNIST); Dermatology (DermaMNIST); Hematology (BloodMNIST); Pathology (PCAM [51], LC25000 [2], PathMNIST); Neuropathology (Amyloid CAA/Diffuse [53]); Histology (TissueMNIST); and Non-clinical Biology (Pollen [1]). For classification tasks, the average accuracy is reported. For retrieval tasks, bidirectional (image-to-text and text-to-image) performance is evaluated using  $R@1$  recall metric. Further details are provided in App. F.

**Baselines.** We select a total of seven data selection baselines for comparison, including (1) **random selection**, which selects samples uniformly from the training pool without any selective control; (2) three **heuristics-based methods**: CLIPScore [21], Concept-Balance, and Concept-Filter [36]; (3) **Influence-based methods**: Dot [67], TracIn [43], and TRAK [40]. Moreover, we also include three commonly used medical-specific CLIP models for reference: PubMedCLIP [10], BioMedCLIP [64], and BMCLIP [36]. Implementation details of all baseline methods and our CHIPS method are provided in App. C.

### 3.2. Main Results

**Effectiveness of CHIPS.** As shown in Tab. 2, across all retention ratios, CHIPS achieves the best average performance on 17 medical tasks among data selection methods, with Medical Avg scores of 27.03, 28.20, and 29.96, exceeding the second-best method by +0.57, +1.57, and +3.68 points, respectively. Notably, with only 10% of the full BIOMEDICA, CHIPS outperforms a 50% random subset (27.03 vs. 26.26); with 30%, it achieves **95.1%** of the full-dataset performance (29.96 vs. 31.51). It is also competitive with specialized medical CLIP models pre-trained on larger datasets: at  $r = 30\%$ , CHIPS slightly surpasses BMCLIP (29.96 vs. 29.86) and consistently outperforms PubMedCLIP and BioMedCLIP across  $r$ . Even though CHIPS is not uniformly best on every specialty, it yields the highest overall average. Importantly, CHIPS better preserves general-domain abilities than the previous SOTA selection method TracIn: for *CLS*, CHIPS retains 90.1%, 89.3%, and 87.2% of the vanilla model at  $r = 10\%, 20\%, 30\%$  (vs. 88.9%, 88.0%, 87.0% for TracIn), and for *RET* it is comparable, slightly lower at  $r = 10\%$  but higher at  $r \geq 20\%$ , yielding a higher average RET across retention ratios. Overall, CHIPS delivers the strongest medical performance while incurring *less* degradation on the general domain than TracIn.

**Generalization abilities of CHIPS.** With a single scoring pass on MetaCLIP-B16-400M (10% kept), we reuse

Model	Medical							General			
	OPH	RAD	DER	HEM	PAT	NEU	HIS	BIO	Avg	CLS	RET
PubMedCLIP	35.92	20.27	9.63	8.45	25.77	60.50	8.45	25.27	26.21	19.05	24.21
BioMedCLIP	14.42	15.59	1.20	10.14	21.17	44.79	4.66	72.91	21.45	7.68	23.55
BMCLIP	38.47	17.44	61.65	9.44	49.75	38.26	5.02	17.28	29.86	57.97	28.27
Vanilla	15.91	19.76	10.82	17.95	30.09	57.96	5.24	10.56	23.51	53.15	29.23
Full Dataset	33.30	12.75	11.72	23.33	49.57	82.79	12.40	9.81	31.51	49.72	24.20
<i>r=10%</i>											
Random	36.01	9.93	11.27	20.61	39.71	43.96	4.68	10.18	24.78	<b>52.21</b>	29.28
Concept-Balance	33.18	12.11	11.67	21.81	40.40	46.82	5.03	10.87	25.50	<u>51.95</u>	<u>30.14</u>
Concept-Filter	31.40	10.81	11.72	23.41	43.14	44.53	5.14	11.06	25.15	51.81	29.19
CLIPScore	15.48	12.75	11.47	20.99	38.23	64.15	5.25	10.56	24.16	53.39	<b>31.27</b>
Dot	42.01	8.54	12.17	16.87	36.98	45.49	4.16	23.51	25.32	48.27	26.47
TracIn	41.30	10.47	12.02	16.69	35.69	51.79	4.96	26.34	<u>26.46</u>	47.26	26.36
TRAK	30.29	12.37	12.17	25.93	39.04	45.95	4.46	12.88	25.19	48.24	27.17
<b>CHIPS (ours)</b>	38.93	11.05	11.87	21.43	37.99	50.22	5.29	25.96	<b>27.03</b>	47.88	25.71
<i>r=20%</i>											
Random	35.79	13.82	11.62	21.92	39.35	36.41	6.60	11.13	25.00	<b>51.39</b>	<u>29.57</u>
Concept-Balance	32.77	13.62	11.97	24.00	44.24	43.16	5.42	10.37	26.20	<u>51.38</u>	<b>30.31</b>
Concept-Filter	31.36	11.70	11.97	25.46	44.98	35.85	6.42	15.21	25.23	51.25	29.54
CLIPScore	17.33	9.83	11.27	18.82	38.01	32.35	4.45	11.25	20.01	51.25	28.81
Dot	39.20	11.19	11.77	13.30	35.46	53.72	5.38	33.63	26.39	47.50	26.93
TracIn	42.47	12.28	11.82	19.70	37.92	46.13	5.07	19.17	<u>26.63</u>	46.79	25.09
TRAK	43.25	10.12	11.02	16.75	37.66	28.83	5.41	28.16	24.54	47.54	25.81
<b>CHIPS (ours)</b>	44.13	13.02	11.87	22.49	40.79	38.54	5.92	30.36	<b>28.20</b>	47.45	25.90
<i>r=30%</i>											
Random	36.77	11.90	12.07	18.42	43.35	47.08	6.42	10.94	<u>26.28</u>	<u>50.98</u>	<b>29.85</b>
Concept-Balance	31.95	11.88	12.07	24.61	42.52	35.88	6.48	10.43	24.56	<b>51.13</b>	<u>29.66</u>
Concept-Filter	32.37	11.23	12.02	25.96	41.40	41.02	6.81	21.06	25.37	50.63	29.54
CLIPScore	21.93	8.25	11.32	13.94	38.81	26.49	4.49	11.94	19.01	50.76	28.09
Dot	38.42	11.05	11.62	15.40	37.52	35.04	7.69	20.74	23.97	46.39	25.67
TracIn	39.63	14.18	11.97	14.24	38.91	41.09	5.69	22.19	25.68	46.23	25.15
TRAK	38.95	10.49	11.42	16.92	36.96	25.70	7.75	25.14	23.54	46.29	24.04
<b>CHIPS (ours)</b>	41.66	13.56	11.37	25.02	43.10	46.53	7.69	36.34	<b>29.96</b>	46.34	26.11
<i>r=50%</i>											
Random	34.47	13.86	11.82	18.82	45.82	41.00	10.06	10.56	26.26	50.56	29.29

Table 2. Downstream performance of MetaCLIP-B16-400M [57] and variants continually pre-trained with data subsets from BIOMEDICA [36] selected by different methods, under a fixed retention ratio  $r \in \{10\%, 20\%, 30\%, 50\%\}$ . Abbreviations: for medical specialties, OPH = Ophthalmology, RAD = Radiology, DER = Dermatology, HEM = Hematology, PAT = Pathology, NEU = Neuropathology, HIS = Histology, BIO = Non-clinical Biology; for metrics in general domain, CLS denotes classification accuracy, and RET denotes the average R@1 across image-to-text and text-to-image retrieval tasks. In each setting, the best result is **bolded** and the second best is underlined.

the computed CHIPS scores to train diverse backbones (B32/B16/L14/H14) and pre-training scales (400M and CC). As shown in Tab. 3, across all seven settings, CHIPS attains the best Medical performance, outperforming TracIn by 0.20-2.65 points. On general-domain metrics, CHIPS typically ranks second (behind Random) and generally matches or exceeds TracIn on CLS and RET, with a single RET exception on B16-400M. Thus, CHIPS transfers across architectures and scales, allowing cached scores to

be reused while delivering strong medical gains with minimal loss of general ability.

**Ablation study.** As shown in Tab. 4, we ablate CHIPS by progressively adding components from Eq. (13). On the medical benchmarks, CHIPS achieves the highest performance at all budgets, surpassing the strongest ablation by +1.05, +0.28, and +1.46 points at  $r = 10\%, 20\%, 30\%$ , respectively. These gains support the multiplicative combina-

Model	Medical CLS	General CLS	General RET
<i>B32-400M</i>			
Random	27.15	<b>49.31</b>	<b>27.33</b>
TracIn	27.48	47.19	25.10
<b>CHIPS (ours)</b>	<b>27.83</b>	<u>47.90</u>	<u>25.65</u>
<i>B32-CC</i>			
Random	27.95	<b>50.69</b>	<b>29.28</b>
TracIn	26.25	48.90	25.72
<b>CHIPS (ours)</b>	<b>28.13</b>	<u>49.48</u>	<u>26.79</u>
<i>B16-400M</i>			
Random	24.78	<b>52.21</b>	<b>29.28</b>
TracIn	26.46	47.26	<u>26.36</u>
<b>CHIPS (ours)</b>	<b>27.03</b>	<u>47.88</u>	25.71
<i>B16-CC</i>			
Random	<u>26.30</u>	<b>55.91</b>	<b>30.16</b>
TracIn	25.89	50.17	27.37
<b>CHIPS (ours)</b>	<b>26.93</b>	<u>51.27</u>	<u>28.17</u>
<i>L14-400M</i>			
Random	<u>29.33</u>	<b>57.07</b>	<b>33.35</b>
TracIn	27.08	52.99	<u>28.17</u>
<b>CHIPS (ours)</b>	<b>29.73</b>	<u>53.65</u>	<u>28.17</u>
<i>L14-CC</i>			
Random	30.75	<b>60.74</b>	<b>32.34</b>
TracIn	<u>31.54</u>	56.98	28.26
<b>CHIPS (ours)</b>	<b>31.74</b>	<u>57.93</u>	<u>30.05</u>
<i>H14-CC</i>			
Random	<u>35.23</u>	<b>61.36</b>	<b>32.82</b>
TracIn	35.10	<u>58.27</u>	31.60
<b>CHIPS (ours)</b>	<b>35.48</b>	58.24	<u>32.09</u>

Table 3. Generalization experiment of MetaCLIP-series adapted models continually pre-trained on 10% kept data from different data selection methods. *400M* denotes the model was pre-trained on 400M general image-text pairs and *CC* denotes the model was pre-trained on 2.5B general image-text pairs.

tion of alignment, learnability, and domain relevance, with the relevance term becoming especially beneficial at larger budgets ( $r = 30\%$ ). Meanwhile, general-domain performance remains close to the best ablation (within  $\leq 0.53$  for General CLS and  $\leq 0.99$  for General RET), indicating minimal trade-off for the medical improvements. On the general domain, the retrieval gap to the best ablation narrows as  $r$  grows ( $0.99 \rightarrow 0.66 \rightarrow 0.37$  for General RET), suggesting controlled specialization towards the target domain rather than catastrophic forgetting.

**Cost analysis.** We measure scoring cost as total FLOPs over  $\mathcal{D}_{\text{pool}}$ . CHIPS requires  $50.9475 \times 10^{15}$  FLOPs, 3.1% lower than TracIn ( $52.5891 \times 10^{15}$ ) and effectively on par with TRAK ( $50.9458 \times 10^{15}$ ). Despite equal-or-lower cost, CHIPS yields consistently stronger medical performance than TracIn (Tab. 2), improving by +0.57, +1.57, and +4.28 points across three retention settings, respectively. In practice, the one-time scoring overhead is further amortized be-

Model	Medical CLS	General CLS	General RET
<i>r=10%</i>			
Alignment-only	25.98	48.33	<b>26.70</b>
Alignment-Margin	25.95	<b>48.41</b>	26.25
<b>CHIPS (ours)</b>	<b>27.03</b>	47.88	25.71
<i>r=20%</i>			
Alignment-only	27.52	46.67	26.25
Alignment-Margin	27.92	<b>46.88</b>	<b>26.56</b>
<b>CHIPS (ours)</b>	<b>28.20</b>	46.73	25.90
<i>r=30%</i>			
Alignment-only	27.84	<b>46.78</b>	25.23
Alignment-Margin	28.50	46.75	<b>25.52</b>
<b>CHIPS (ours)</b>	<b>29.96</b>	46.34	25.15

Table 4. Ablation experiment of CHIPS on MetaCLIP-B16-400M under 10%, 20%, and 30% data retention ratios. *Alignment-only* uses single alignment score, *Alignment-Margin* additionally introduces the margin term, and CHIPS multiplies all three metrics.

cause CHIPS scores can be cached and reused across architectures and pre-training scales (Tab. 3). The full FLOPs computation process is provided in App. G.

## 4. Analysis

### 4.1. Alignment

**Effect of target evaluation set size.** Expanding the target evaluation set  $\mathcal{D}_{\text{eval}}$  sharpens the alignment direction  $\mathbf{u}_\theta$  and improves medical accuracy with minimal general-domain drift. As shown in Fig. 2(A), as samples per task increase from 50 to 200, Medical CLS improves from 26.25 to 27.03 (+0.78), then saturates at 250 (27.12, +0.09). The slight dip at 100 (25.82) reflects higher variance at smaller set sizes, while overall the trend is upward and stabilizing around 200. General CLS remains essentially flat across all sizes (48.41 at 50 to 47.88 at 200; total range  $\leq 0.55$ ), indicating that larger  $\mathcal{D}_{\text{eval}}$  chiefly benefits medical alignment without harming general performance. Balancing diminishing returns beyond 200 against the linear increase in scoring cost, and we adopt 200 samples per task as the default.

### Projection layers dominate alignment with text being more informative.

We ablate the end-point geometry  $\vartheta = \{\mathbf{W}_v, \mathbf{W}_t, \tau\}$  into *All*, *Logit-only*, *Visual-only*, and *Text-only*, with results shown in Fig. 3. Across methods, *Text-only* nearly matches *All* (98.6–99.7%), *Visual-only* lags, and *Logit-only* is weakest. For CHIPS, the scores are 27.03 (*All*), 26.95 (*Text-only*, -0.08; 99.7%), 26.67 (*Visual-only*, -0.36; 98.7%), and 23.83 (*Logit-only*, -3.20). These results show that alignment resides primarily in the projection heads, especially  $\mathbf{W}_t$ , with  $\mathbf{W}_v$  providing a smaller yet complementary gain. Moreover, CHIPS is more robust to projection layers compared with baseline methods, retaining 99.7% (*Text-only*) and 98.7% (*Visual-only*), the highest

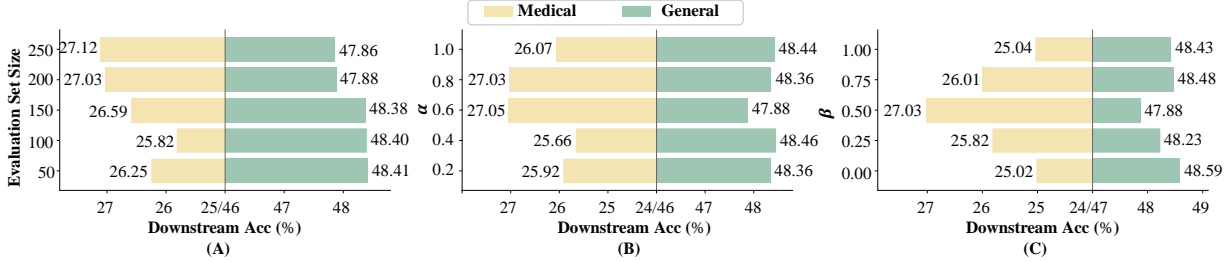


Figure 2. Downstream results of MetaCLIP-B16-400M continually pre-trained on 10% data selected from CHIPS under: (A) different evaluation set sizes, (B) different mixing  $\alpha$  in computing alignment scores, and (C) different balance  $\beta$  in computing relevance scores.

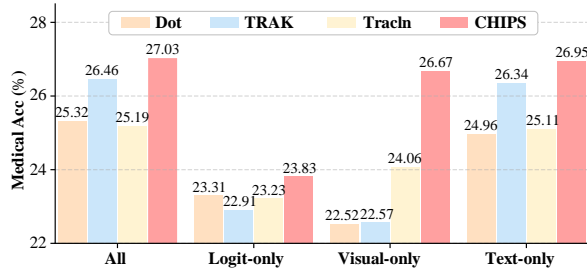


Figure 3. Medical downstream results of MetaCLIP-B16-400M continually pre-trained on 10% data selected from different selection methods under various end-point geometry settings.

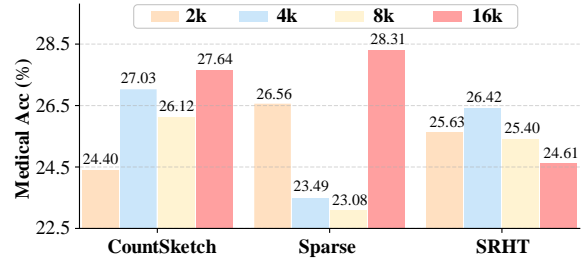


Figure 4. Medical downstream results of MetaCLIP-B16-400M continually pre-trained on 10% data selected from CHIPS under various random projection settings.

among methods, and exhibiting the smallest text–visual gap (0.28 vs. 2.43/3.77/1.05 for Dot/Tracln/TRAK).

**Effect of random projection.** We compare three random projection methods in computing the alignment score  $\hat{A}_\alpha(z)$  and vary the target dimension  $k \in \{2048, 4096, 8192, 16384\}$ , with results shown in Fig. 4. *Sparse* projections are the most effective, peaking at 28.31 (16k) and remaining strong even at 2k (26.56). *CountSketch* improves with dimension (24.40→27.64 from 2k to 16k), with a small dip at 8k (26.12); at 4k it already reaches 27.03. *SRHT* is less robust, peaking at 4k (26.42) and degrading at 16k (24.61). Overall, *Sparse*–16k is best (+0.67 over *CountSketch*–16k; +1.89 over *SRHT*–4k). For tighter budgets, *CountSketch*–4k offers a cost-efficient alternative within about 1.3 points of the best.

**Balancing positive and negative curvature.** In Eq. (8),  $\alpha$  linearly mixes positive and negative pair curvature to form  $\mathbf{M}$ , which reweights gradients in  $A(z) = \mathbf{g}_\vartheta(z)^\top \mathbf{M}^{-1} \mathbf{u}_\vartheta$ . As shown in Fig. 2(B), Medical CLS peaks at  $\alpha=0.6$  (27.05) and remains essentially tied at 0.8 (27.03), while both smaller (0.2: 25.92; 0.4: 25.66) and larger (1.0: 26.07) values underperform by about 1–1.4 points. General CLS is almost flat across  $\alpha$  (48.36–48.46), with a modest dip at 0.6 (47.88), indicating that  $\alpha$  mainly governs target-domain discrimination with negligible general-domain impact. Mech-

anistically, moderate  $\alpha$  balances attraction to positives and repulsion from negatives, improving the conditioning of  $\mathbf{M}$  and yielding a more discriminative alignment direction; extremes overweight one term and reduce  $A(z)$ ’s utility. We therefore recommend  $\alpha \in [0.6, 0.8]$  (default 0.6 for medical focus; 0.4 if slightly prioritizing general-domain retention).

## 4.2. Domain Relevance and General Retention

In Eq. (12),  $\beta$  balances visual and textual similarities when computing  $w_R(z)$ . As shown in Fig. 2(C), varying  $\beta \in \{0, 0.25, 0.5, 0.75, 1\}$  reveals a clear adaptation–retention trade-off: Medical CLS peaks at  $\beta=0.5$  (27.03), improving by 2.01–1.21 points over the unimodal extremes ( $\beta=0$ : 25.02;  $\beta=1$ : 25.04). In contrast, General CLS is flat-tish (48.59→47.88 across settings; total spread 0.71), with the best retention at the extremes ( $\beta=0$ : 48.59;  $\beta=1$ : 48.43) and the largest dip at  $\beta=0.5$  (47.88). This U-shaped retention pattern indicates that balanced relevance sharpens specialization to the medical target, whereas unimodal weighting selects more generic samples that better preserve general-domain ability. A slight skew toward text ( $\beta=0.75$ ) offers a good compromise: 26.01 on Medical (within 1.02 of the best) with near-top 48.48 on General, which is consistent with our end-point geometry ablation where text signals are more informative (Sec. 4.1). Finally, the overall narrow range in General CLS ( $\leq 0.71$ ) aligns with the bounded-drift property of  $w_R$ , which limits deviation from

the base alignment distribution. We adopt  $\beta=0.5$  for maximal target-domain gains and recommend  $\beta \approx 0.75$  when general retention is a priority.

## 5. Conclusion

We propose CHIPS, showing that principled data selection can substitute for raw scale in CLIP continual pre-training. On 17 medical benchmarks, CHIPS attains SOTA performance among selection baselines, matches full-dataset CPT with 30% of the data, and outperforms half-dataset CPT using only 10%. Across 31 general-domain benchmarks, it yields the smallest performance drop under 10–30% retention ratios, better preserving general capabilities. Limitations include reliance on a target validation distribution, we will explore unlabeled or shift-robust target signals and extensions beyond the CLIP model in the future work.

## References

- [1] Sebastiano Battiato, Alessandro Ortis, Francesca Trenta, Lorenzo Ascari, Mara Politi, and Consolata Siniscalco. Pollen13k: a large scale microscope pollen grain image dataset. In *2020 IEEE International Conference on Image Processing (ICIP)*, pages 2456–2460. IEEE, 2020. 5, 9
- [2] Andrew A Borkowski, Marilyn M Bui, L Brannon Thomas, Catherine P Wilson, Lauren A DeLand, and Stephen M Mastorides. Lung and colon cancer histopathological image dataset (lc25000). *arXiv preprint arXiv:1912.12142*, 2019. 5, 9
- [3] Lukas Bossard, Matthieu Guillaumin, and Luc Van Gool. Food-101 – mining discriminative components with random forests. In *European Conference on Computer Vision (ECCV)*, 2014. 5, 8
- [4] Yuyan Chen, Nico Lang, B. Christian Schmidt, Aditya Jain, Yves Basset, Sara Beery, Maxim Larrivé, and David Rolnick. Open-set recognition of novel species in biodiversity monitoring, 2025. 1
- [5] Gong Cheng, Junwei Han, and Xiaoqiang Lu. Remote sensing image scene classification: Benchmark and state of the art. *Proceedings of the IEEE*, 105(10):1865–1883, 2017. 5, 9
- [6] Mircea Cimpoi, Subhansu Maji, Iasonas Kokkinos, Sammy Mohamed, and Andrea Vedaldi. Describing textures in the wild. In *Proceedings of the IEEE conference on computer vision and pattern recognition*, pages 3606–3613, 2014. 5, 9
- [7] Adam Coates, Andrew Y. Ng, and Honglak Lee. An analysis of single-layer networks in unsupervised feature learning. In *International Conference on Artificial Intelligence and Statistics (AISTATS)*, 2011. Introduces the STL-10 dataset. 5, 8
- [8] Jia Deng, Wei Dong, Richard Socher, Li-Jia Li, Kai Li, and Li Fei-Fei. Imagenet: A large-scale hierarchical image database. In *IEEE Conference on Computer Vision and Pattern Recognition (CVPR)*, pages 248–255, 2009. 5, 7
- [9] Junwei Deng, Yuzheng Hu, Pingbang Hu, Ting-wei Li, Shixuan Liu, Jiachen T. Wang, Dan Ley, Qirun Dai, Benhao Huang, Jin Huang, Cathy Jiao, Hoang Anh Just, Yijun Pan, Jingyan Shen, Yiwen Tu, Weiyi Wang, Xinhe Wang, Shichang Zhang, Shiyuan Zhang, Ruoxi Jia, Himabindu Lakkaraju, Hao Peng, Weijing Tang, Chenyan Xiong, Jieyu Zhao, Hanghang Tong, Han Zhao, and Jiaqi W. Ma. A survey of data attribution: Methods, applications, and evaluation in the era of generative ai. *SSRN Electronic Journal*, 2025. 1
- [10] Sedigheh Eslami, Christoph Meinel, and Gerard de Melo. PubMedCLIP: How much does CLIP benefit visual question answering in the medical domain? In *Findings of the Association for Computational Linguistics: EACL 2023*, pages 1181–1193, Dubrovnik, Croatia, 2023. Association for Computational Linguistics. 5
- [11] Philipp Eulenberg, Niklas Köhler, Thomas Blasi, Andrew Filby, Anne E Carpenter, Paul Rees, Fabian J Theis, and F Alexander Wolf. Reconstructing cell cycle and disease progression using deep learning. *Nature communications*, 8(1): 463, 2017. 5, 9
- [12] Mark Everingham, Luc Van Gool, Christopher K. I. Williams, John Winn, and Andrew Zisserman. The pascal visual object classes (voc) challenge. *International Journal of Computer Vision (IJCV)*, 88(2):303–338, 2010. 5, 8
- [13] Li Fei-Fei, Rob Fergus, and Pietro Perona. Learning generative visual models from few training examples: An incremental bayesian approach tested on 101 object categories. In *CVPR 2004, Workshop on Generative-Model Based Vision*, 2004. 5, 8
- [14] Andreas Geiger, Philip Lenz, and Raquel Urtasun. Vision meets robotics: The kitti dataset. *International Journal of Robotics Research (IJRR)*, 2013. 5, 8
- [15] Zahra Gharraee, Scott C. Lowe, ZeMing Gong, Pablo Millan Arias, Nicholas Pellegrino, Austin T. Wang, Joakim Bruslund Haurum, Iuliia Zarubiieva, Lila Kari, Dirk Steinke, Graham W. Taylor, Paul Fieguth, and Angel X. Chang. Bioscan5m: A multimodal dataset for insect biodiversity. In *Advances in Neural Information Processing Systems*, pages 36285–36313. Curran Associates, Inc., 2024. 1
- [16] Ian J Goodfellow, Dumitru Erhan, Pierre Luc Carrier, Aaron Courville, Mehdi Mirza, Ben Hamner, Will Cukierski, Yichuan Tang, David Thaler, Dong-Hyun Lee, et al. Challenges in representation learning: A report on three machine learning contests. In *International conference on neural information processing*, pages 117–124. Springer, 2013. 5
- [17] Jianyang Gu, Samuel Stevens, Elizabeth G Campolongo, Matthew J Thompson, Net Zhang, Jiaman Wu, Andrei Kopanev, Zheda Mai, Alexander E White, James Balhoff, et al. Bioclip 2: Emergent properties from scaling hierarchical contrastive learning. *arXiv preprint arXiv:2505.23883*, 2025. 1
- [18] Haoyu He, Jianfei Cai, Jing Zhang, Dacheng Tao, and Bohan Zhuang. Sensitivity-aware visual parameter-efficient fine-tuning. In *Proceedings of the IEEE/CVF International Conference on Computer Vision*, pages 11825–11835, 2023. 1
- [19] Patrick Helber, Benjamin Bischke, Andreas Dengel, and Damian Borth. Eurosat: A novel dataset and deep learning benchmark for land use and land cover classification. *IEEE Journal of Selected Topics in Applied Earth Observations and Remote Sensing*, 12(7):2217–2226, 2019. 5, 8

- [20] Dan Hendrycks, Kevin Zhao, Steven Basart, Jacob Steinhardt, and Dawn Song. Natural adversarial examples. *arXiv preprint arXiv:1907.07174*, 2019. 5, 8
- [21] Jack Hessel, Ari Holtzman, Maxwell Forbes, Ronan Le Bras, and Yejin Choi. CLIPScore: A reference-free evaluation metric for image captioning. In *Proceedings of the 2021 Conference on Empirical Methods in Natural Language Processing*, pages 7514–7528, Online and Punta Cana, Dominican Republic, 2021. Association for Computational Linguistics. 5, 4
- [22] Micah Hodosh, Peter Young, and Julia Hockenmaier. Framing image description as a ranking task: Data, models and evaluation metrics. *J. Artif. Intell. Res.*, 47:853–899, 2013. 5, 9
- [23] Wisdom Oluchi Ikezogwo, Mehmet Saygin Seyfioglu, Fate-meh Ghezloo, Dylan Stefan Chan Geva, Fatwir Sheikh Mohammed, Pavan Kumar Anand, Ranjay Krishna, and Linda Shapiro. Quilt-1m: One million image-text pairs for histopathology, 2025. 1
- [24] Sajid Javed, Arif Mahmood, Iyyakutti Iyappan Ganapathi, Fayaz Ali Dharejo, Naoufel Werghi, and Mohammed Ben-namoun. Cclip: Zero-shot learning for histopathology with comprehensive vision-language alignment. In *Proceedings of the IEEE/CVF conference on computer vision and pattern recognition*, pages 11450–11459, 2024. 1
- [25] Saurav Jha, Dong Gong, and Lina Yao. Clap4clip: Continual learning with probabilistic finetuning for vision-language models. In *Advances in Neural Information Processing Systems*, pages 129146–129186. Curran Associates, Inc., 2024. 1
- [26] Justin Johnson, Bharath Hariharan, Laurens van der Maaten, Li Fei-Fei, C. Lawrence Zitnick, and Ross Girshick. Clevr: A diagnostic dataset for compositional language and elementary visual reasoning. In *IEEE Conference on Computer Vision and Pattern Recognition (CVPR)*, 2017. 5, 9
- [27] SungYub Kim, Kyungsu Kim, and Eunho Yang. GEX: A flexible method for approximating influence via geometric ensemble. In *Thirty-seventh Conference on Neural Information Processing Systems*, 2023. 2, 1
- [28] Pang Wei Koh and Percy Liang. Understanding black-box predictions via influence functions. In *International conference on machine learning*, pages 1885–1894. PMLR, 2017. 1
- [29] Jonathan Krause, Jia Deng, Michael Stark, and Li Fei-Fei. Collecting a large-scale dataset of fine-grained cars. In *Proceedings of the IEEE Conference on Computer Vision and Pattern Recognition Workshops (FGVC)*, 2013. 5, 8
- [30] Alex Krizhevsky. Learning multiple layers of features from tiny images. Technical report, University of Toronto, 2009. 5, 8
- [31] Yann LeCun, Corinna Cortes, and Christopher J.C. Burges. The mnist database of handwritten digits. <http://yann.lecun.com/exdb/mnist/>, 1998. 5, 8
- [32] Yann LeCun, Fu Jie Huang, and Léon Bottou. Learning methods for generic object recognition with invariance to pose and lighting. In *IEEE Conference on Computer Vision and Pattern Recognition (CVPR)*, 2004. 5, 8
- [33] Tsung-Yi Lin, Michael Maire, Serge J. Belongie, James Hays, Pietro Perona, Deva Ramanan, Piotr Dollár, and C. Lawrence Zitnick. Microsoft COCO: common objects in context. In *Computer Vision - ECCV 2014 - 13th European Conference, Zurich, Switzerland, September 6-12, 2014, Proceedings, Part V*, pages 740–755. Springer, 2014. 5, 9
- [34] Weixiong Lin, Ziheng Zhao, Xiaoman Zhang, Chaoyi Wu, Ya Zhang, Yanfeng Wang, and Weidi Xie. Pmc-clip: Contrastive language-image pre-training using biomedical documents. In *International Conference on Medical Image Computing and Computer-Assisted Intervention*, pages 525–536. Springer, 2023. 1
- [35] Weiyang Liu, Zeju Qiu, Yao Feng, Yuliang Xiu, Yuxuan Xue, Longhui Yu, Haiwen Feng, Zhen Liu, Juyeon Heo, Songyou Peng, et al. Parameter-efficient orthogonal finetuning via butterfly factorization. In *ICLR*, 2024. 1
- [36] Alejandro Lozano, Min Woo Sun, James Burgess, Liangyu Chen, Jeffrey J Nirschl, Jeffrey Gu, Ivan Lopez, Josiah Aklilu, Anita Rau, Austin Wolfgang Katzer, et al. Biomedica: An open biomedical image-caption archive, dataset, and vision-language models derived from scientific literature. In *Proceedings of the Computer Vision and Pattern Recognition Conference*, pages 19724–19735, 2025. 1, 4, 5, 6, 10
- [37] Subhansu Maji, Esa Rahtu, Juho Kannala, Matthew Blaschko, and Andrea Vedaldi. Fine-grained visual classification of aircraft. *arXiv preprint arXiv:1306.5151*, 2013. 5, 8
- [38] Yuval Netzer, Tao Wang, Adam Coates, Alessandro Bis-sacco, Bo Wu, and Andrew Y. Ng. Reading digits in natural images with unsupervised feature learning. Technical report, Stanford University, 2011. 5, 8
- [39] Maria-Emma Nilsback and Andrew Zisserman. Automated flower classification over a large number of classes. In *Indian Conference on Computer Vision, Graphics and Image Processing (ICVGIP)*, 2008. 5, 8
- [40] Sung Min Park, Kristian Georgiev, Andrew Ilyas, Guillaume Leclerc, and Aleksander Madry. TRAK: Attributing model behavior at scale. In *Proceedings of the 40th International Conference on Machine Learning*, pages 27074–27113. PMLR, 2023. 5
- [41] Omkar M. Parkhi, Andrea Vedaldi, Andrew Zisserman, and C. V. Jawahar. Cats and dogs. In *IEEE Conference on Computer Vision and Pattern Recognition (CVPR)*, pages 3498–3505, 2012. 5, 8
- [42] Mansheej Paul, Surya Ganguli, and Gintare Karolina Dziugaite. Deep learning on a data diet: Finding important examples early in training. In *Advances in Neural Information Processing Systems*, pages 20596–20607. Curran Associates, Inc., 2021. 2, 1
- [43] Garima Pruthi, Frederick Liu, Satyen Kale, and Mukund Sundararajan. Estimating training data influence by tracing gradient descent. In *Advances in Neural Information Processing Systems*, pages 19920–19930. Curran Associates, Inc., 2020. 2, 5, 1
- [44] Alec Radford, Jong Wook Kim, Chris Hallacy, Aditya Ramesh, Gabriel Goh, Sandhini Agarwal, Girish Sastry,

- Amanda Askeel, Pamela Mishkin, Jack Clark, et al. Learning transferable visual models from natural language supervision. In *International conference on machine learning*, pages 8748–8763. PmLR, 2021. 1, 2, 5, 9
- [45] Benjamin Recht, Rebecca Roelofs, Ludwig Schmidt, and Vaishaal Shankar. Do imagenet classifiers generalize to imagenet? In *International Conference on Machine Learning (ICML)*, 2019. 5, 8
- [46] Sreetama Sarkar, Souvik Kundu, Kai Zheng, and Peter A. Beerel. Block selective reprogramming for on-device training of vision transformers. In *2024 IEEE/CVF Conference on Computer Vision and Pattern Recognition Workshops (CVPRW)*, pages 8094–8103, 2024. 1
- [47] Andrea Schioppa, Polina Zablotskaia, David Vilar, and Artem Sokolov. Scaling up influence functions. *Proceedings of the AAAI Conference on Artificial Intelligence*, 36(8):8179–8186, 2022. 2, 1
- [48] Danli Shi, Weiyi Zhang, Jiancheng Yang, Siyu Huang, Xiaolan Chen, Pusheng Xu, Kai Jin, Shan Lin, Jin Wei, Mayinuer Yusufu, Shunming Liu, Qing Zhang, Zongyuan Ge, Xun Xu, and Mingguang He. A multimodal visual–language foundation model for computational ophthalmology. *npj Digital Medicine*, 8(1):381, 2025. 1
- [49] Johannes Stalkamp, Marc Schlipsing, Jan Salmen, and Christian Igel. The german traffic sign recognition benchmark: A multi-class classification dataset. In *International Joint Conference on Neural Networks (IJCNN)*, 2011. 5
- [50] Samuel Stevens, Jiaman Wu, Matthew J Thompson, Elizabeth G Campolongo, Chan Hee Song, David Edward Carlyn, Li Dong, Wasila M Dahdul, Charles Stewart, Tanya Berger-Wolf, et al. Bioclip: A vision foundation model for the tree of life. In *Proceedings of the IEEE/CVF conference on computer vision and pattern recognition*, pages 19412–19424, 2024. 1
- [51] Bastiaan S Veeling, Jasper Linmans, Jim Winkens, Taco Cohen, and Max Welling. Rotation equivariant cnns for digital pathology. In *International Conference on Medical image computing and computer-assisted intervention*, pages 210–218. Springer, 2018. 5, 9
- [52] Xiaosong Wang, Yifan Peng, Le Lu, Zhiyong Lu, Mohammadhadi Bagheri, and Ronald M Summers. Chestx-ray8: Hospital-scale chest x-ray database and benchmarks on weakly-supervised classification and localization of common thorax diseases. In *Proceedings of the IEEE conference on computer vision and pattern recognition*, pages 2097–2106, 2017. 5, 9
- [53] D. R. Wong, Z. Tang, N. C. Mew, et al. Deep learning from multiple experts improves identification of amyloid neuropathologies. *Acta Neuropathologica Communications*, 10(66), 2022. 5, 9
- [54] Junjie Wu, Jiangtao Xie, Zhaolin Zhang, Qilong Wang, Qinghua Hu, Peihua Li, and Sen Xu. Dalip: Distribution alignment-based language-image pre-training for domain-specific data, 2025. 1
- [55] Jianxiong Xiao, James Hays, Krista A. Ehinger, Aude Oliva, and Antonio Torralba. Sun database: Large-scale scene recognition from abbey to zoo. In *IEEE Conference on Computer Vision and Pattern Recognition (CVPR)*, 2010. 5, 8
- [56] Yunfei Xie, Ce Zhou, Lang Gao, Juncheng Wu, Xianhang Li, Hong-Yu Zhou, Sheng Liu, Lei Xing, James Zou, Cihang Xie, and Yuyin Zhou. Medtrinity-25m: A large-scale multimodal dataset with multigranular annotations for medicine. In *The Thirteenth International Conference on Learning Representations*, 2025. 5, 12, 30
- [57] Hu Xu, Saining Xie, Xiaoqing Tan, Po-Yao Huang, Russell Howes, Vasu Sharma, Shang-Wen Li, Gargi Ghosh, Luke Zettlemoyer, and Christoph Feichtenhofer. Demystifying CLIP data. In *The Twelfth International Conference on Learning Representations*, 2024. 5, 6
- [58] Shin’ya Yamaguchi, Dewei Feng, Sekitoshi Kanai, Kazuki Adachi, and Daiki Chijiwa. Post-pre-training for modality alignment in vision-language foundation models. In *Proceedings of the Computer Vision and Pattern Recognition Conference*, pages 4256–4266, 2025. 1
- [59] Siyuan Yan, Zhen Yu, Clare Primiero, Cristina Vico-Alonso, Zhonghua Wang, Litao Yang, Philipp Tschandl, Ming Hu, Lie Ju, Gin Tan, Vincent Tang, Aik Beng Ng, David Powell, Paul Bonnington, Simon See, Elisabetta Magnaterra, Peter Ferguson, Jennifer Nguyen, Pascale Guitera, Jose Banuls, Monika Janda, Victoria Mar, Harald Kittler, H. Peter Soyer, and Zongyuan Ge. A multimodal vision foundation model for clinical dermatology. *Nature Medicine*, 31(8):2691–2702, 2025. 1
- [60] Chih-Hsuan Yang, Ben Feuer, Zaki Jubery, Zi K. Deng, Andre Nakkab, Zahid Hasan, Shivani Chiranjeevi, Kelly Marshall, Nirmal Baishnab, Asheesh K Singh, Arti Singh, Soumik Sarkar, Nirav Merchant, Chinmay Hegde, and Baskar Ganapathysubramanian. Biotrove: A large curated image dataset enabling ai for biodiversity. In *Advances in Neural Information Processing Systems*, pages 102101–102120. Curran Associates, Inc., 2024. 1
- [61] Jiancheng Yang, Rui Shi, Donglai Wei, Zequan Liu, Lin Zhao, Bilian Ke, Hanspeter Pfister, and Bingbing Ni. Medmnist v2-a large-scale lightweight benchmark for 2d and 3d biomedical image classification. *Scientific Data*, 10(1):41, 2023. 5, 9
- [62] Xichen Ye, Yifan Wu, WEIZHONG ZHANG, Cheng Jin, and Yifan Chen. Towards robust influence functions with flat validation minima. In *Forty-second International Conference on Machine Learning*, 2025. 2, 1
- [63] Peter Young, Alice Lai, Micah Hodosh, and Julia Hockenmaier. From image descriptions to visual denotations: New similarity metrics for semantic inference over event descriptions. *Transactions of the Association for Computational Linguistics*, 2:67–78, 2014. 5, 9
- [64] Sheng Zhang, Yanbo Xu, Naoto Usuyama, Hanwen Xu, Jaspreet Bagga, Robert Tinn, Sam Preston, Rajesh Rao, Mu Wei, Naveen Valluri, Cliff Wong, Andrea Tupini, Yu Wang, Matt Mazzola, Swadheen Shukla, Lars Liden, Jianfeng Gao, Angela Crabtree, Brian Piening, Carlo Bifulco, Matthew P. Lungren, Tristan Naumann, Sheng Wang, and Hoifung Poon. Biomedclip: a multimodal biomedical foundation model pre-trained from fifteen million scientific image-text pairs, 2025. 1, 5
- [65] Yi Zhang, Yi-Xuan Deng, Meng-Hao Guo, and Shi-Min Hu. Adaptive parameter selection for tuning vision-language

- models. In *Proceedings of the IEEE/CVF Conference on Computer Vision and Pattern Recognition (CVPR)*, pages 4280–4290, 2025. 1
- [66] Zihao Zhao, Yuxiao Liu, Han Wu, Mei Wang, Yonghao Li, Sheng Wang, Lin Teng, Disheng Liu, Zhiming Cui, Qian Wang, et al. Clip in medical imaging: A survey. *Medical Image Analysis*, page 103551, 2025. 1
- [67] Xinlin Zhuang, Feilong Tang, Haolin Yang, Xiwei Liu, Ming Hu, Huifa Li, Haochen Xue, Junjun He, Zongyuan Ge, Yichen Li, Ying Qian, and Imran Razzak. Towards efficient medical reasoning with minimal fine-tuning data. *arXiv preprint arXiv:2508.01450*, 2025. 5

# CHIPS: Efficient CLIP Adaptation via Curvature-aware Hybrid Influence-based Data Selection

## Supplementary Material

### Appendix Contents

A. Related Work	1
B. Proofs	1
B.1. Alignment Direction	2
B.2. Proxy Alignment in Subspace	2
B.3. Negative Pair Curvature	3
C. Data Selection Implementation Details	3
C.1. Problem Setup	3
C.2. CHIPS	4
C.3. Heuristics-based Baselines	4
C.4. Influence-based Baselines in the End-point Subspace	5
D. Score Distribution	5
E. Training	5
E.1. Software and Distributed Setup	5
E.2. Data Preprocessing and Batching	5
E.3. Optimization Schedule	5
E.4. Counting Steps and Budget Fairness	6
F. Evaluation	7
F.1. General-Domain Datasets	7
F.2. Medical-Domain Datasets	9
G. FLOPs Computation	10
G.1. Numerical Totals	10
G.2. Assumptions and Further notes	10
H. Full Results	10
H.1. Main Experiment	10
H.2. Generalization Experiment	12
H.3. Ablation Experiment	12
H.4. Analysis Experiment	12
I. Additional Results	12

### A. Related Work

**CLIP Adaptation.** Current approaches for effective CLIP adaptation to specialized vertical domains (e.g., Medical) can be broadly categorized into two paradigms: model-centric and data-centric methods [66]. Model-centric approaches primarily focus on developing novel training strategies, including probabilistic fine-tuning [25] and many-to-many contrastive learning [24], as well as parameter-efficient fine-tuning (PEFT) techniques [18, 46, 58, 65]. In contrast, data-centric approaches emphasize the collection of large-scale domain-specific datasets for continual pre-training. Within the general-purpose medical domain, PMC-CLIP [34] leveraged approximately 2M samples, BioMedCLIP [64] curated 15M samples, BIOMED-ICA [36] assembled 24M samples, and MedTrinity aggre-

gated 25M samples. For more specialized medical subdomains, QUILT [23] compiled 1M samples for Histopathology, EYECLIP [48] gathered approximately 3M samples for Ophthalmology, and PanDerm [59] curated 2M samples for Dermatology. In the biology and biodiversity domains, even larger-scale datasets ranging from 5M to 214M samples have been collected [4, 15, 17, 50, 54, 60]. In this work, rather than pursuing resource-intensive dataset scaling, we investigate the intrinsic characteristics of existing domain-specific datasets and employ strategic data selection to achieve more efficient CLIP adaptation.

**Data Attribution.** Data attribution methods quantify the influence of individual training samples on model training efficacy. [28] initially introduced Influence Functions (IF), proposing the LiSSA approximation to efficiently compute the inverse Hessian-vector product, wherein the computation entails calculating the Hessian inverse, iterating through validation and training samples, and deriving influence scores through gradient-based calculations. [43] proposed TracIn, which offers a more intuitive first-order approximation that tracks model training dynamics across multiple checkpoints. [42] introduced EL2N, a self-influence metric that computes the L2 norm of prediction error vectors without requiring explicit validation samples. [47] proposed the Arnoldi iteration method, which leverages dominant eigenvalue decomposition to address the computational overhead and non-H-invariance issues inherent in random projection approaches. [27] introduced GEX, reformulating IF to capture bimodal influence distributions by replacing gradient-based Taylor approximations with direct loss multiplications and employing ensemble models to mitigate Hessian singularity bias. [62] proposed FVM, which optimizes for flat validation minima to enhance the stability of influence estimations for mislabeled sample detection. In this work, we propose an IF variant specifically tailored for CLIP influence estimation.

### B. Proofs

This section provides consolidated derivations and proofs for the three core components referenced in Sec. 2.1, Sec. 2.2, and Sec. 2.3. Unless stated otherwise, expectations are taken over the mini-batch sampling and data randomness at the current parameter iterate  $\theta$ . We write  $\hat{\mathbf{g}} = \frac{1}{B} \sum_{i=1}^B \nabla_{\theta} \ell(z_i; \theta)$ ,  $\mathbf{g}_q = \mathbb{E}_{z \sim q} [\nabla_{\theta} \ell(z; \theta)]$ ,  $\mathbf{u} = \nabla_{\theta} \mathcal{L}_{\text{eval}}(\theta)$ , and use the Euclidean inner product and norm. Spectral and Frobenius norms are denoted by  $\|\cdot\|_2$  and  $\|\cdot\|_F$ .

## B.1. Alignment Direction

In a neighborhood of  $\theta$  assume either (i)  $\mathcal{L}_{\text{eval}} \in C^2$  with Hessian-Lipschitz constant  $L_H$ , or (ii)  $\mathcal{L}_{\text{eval}}$  is  $\rho$ -smooth.

**Second-order upper bound.** For  $\Delta\theta$ , the second-order Taylor expansion with integral remainder gives

$$\begin{aligned} \mathcal{L}_{\text{eval}}(\theta + \Delta\theta) &= \mathcal{L}_{\text{eval}}(\theta) + \mathbf{u}^\top \Delta\theta \\ &+ \frac{1}{2} \Delta\theta^\top \mathbf{H}_{\text{eval}}(\Theta) \Delta\theta + R_3, \end{aligned} \quad (14)$$

where  $\Theta$  lies on the segment between  $\theta$  and  $\theta + \Delta\theta$ , and  $|R_3| \leq \frac{L_H}{6} \|\Delta\theta\|^3$ . With the one-step SGD move  $\Delta\theta = -\eta \hat{\mathbf{g}}$  and taking expectation,

$$\begin{aligned} \mathbb{E}[\Delta\mathcal{L}_{\text{eval}}] &\leq -\eta \mathbf{g}_q^\top \mathbf{u} \\ &+ \frac{1}{2} \eta^2 \mathbb{E}[\hat{\mathbf{g}}^\top \mathbf{H}_{\text{eval}}(\Theta) \hat{\mathbf{g}}] \\ &+ \frac{L_H}{6} \eta^3 \mathbb{E}[\|\hat{\mathbf{g}}\|^3], \end{aligned}$$

which matches Eq. (2) in the main text and shows that descent is driven by the alignment term  $-\mathbf{g}_q^\top \mathbf{u}$ .

**First-order upper bound.** If  $\mathcal{L}_{\text{eval}}$  is  $\rho$ -smooth, the Descent Lemma yields

$$\mathcal{L}_{\text{eval}}(\theta + \Delta\theta) \leq \mathcal{L}_{\text{eval}}(\theta) + \mathbf{u}^\top \Delta\theta + \frac{\rho}{2} \|\Delta\theta\|^2. \quad (15)$$

Setting  $\Delta\theta = -\eta \hat{\mathbf{g}}$  and taking expectations gives Eq. (3).

Regarding mini-batch variance, let  $\Sigma_q = \text{Cov}_{z \sim q}[\nabla_\theta \ell(z; \theta)]$ , then

$$\begin{aligned} \mathbb{E}[\|\hat{\mathbf{g}}\|^2] &= \|\mathbf{g}_q\|^2 + \frac{1}{B} \text{tr}(\Sigma_q), \\ \mathbb{E}[\|\hat{\mathbf{g}} - \mathbf{g}_q\|^2] &= \frac{1}{B} \text{tr}(\Sigma_q). \end{aligned} \quad (16)$$

This makes explicit how the batch size  $B$  moderates the quadratic term in Eq. (3). In a local quadratic model the steepest descent direction for  $\mathcal{L}_{\text{eval}}$  is  $\mathbf{H}_{\text{eval}}^{-1} \mathbf{u}$ . Hence a selection distribution  $q$  that increases  $\mathbf{g}_q^\top \mathbf{H}_{\text{eval}}^{-1} \mathbf{u}$  is desirable, which motivates the proxy alignment in Sec. 2.2.

**AdamW-aware form.** At iteration  $t$ , let  $\mathbf{g}_t = \frac{1}{B} \sum_{i=1}^B \nabla_\theta \ell(z_i; \theta_t)$ . Consider Adam moments and bias corrections as the following forms

$$\begin{aligned} m_t &= \beta_1 m_{t-1} + (1 - \beta_1) \mathbf{g}_t, \\ v_t &= \beta_2 v_{t-1} + (1 - \beta_2) (\mathbf{g}_t \odot \mathbf{g}_t), \\ \hat{m}_t &= \frac{m_t}{1 - \beta_1^t}, \\ \hat{v}_t &= \frac{v_t}{1 - \beta_2^t}, \\ \mathbf{P}_t &= \text{diag}((\sqrt{\hat{v}_t} + \epsilon)^{-1}), \end{aligned}$$

where  $\odot$  denotes the element-wise product. With decoupled weight decay  $w_d > 0$  and diagonal mask  $\mathbf{D}$ , the update is

$$\Delta\theta_t \triangleq \theta_{t+1} - \theta_t = -\eta_t (\mathbf{P}_t \hat{m}_t + w_d \mathbf{D} \theta_t).$$

Under the  $C^2$  and Hessian-Lipschitz assumption, Eq. (14) gives

$$\begin{aligned} \mathbb{E}[\Delta\mathcal{L}_{\text{eval}}] &\leq -\eta_t \mathbb{E}[\hat{m}_t^\top \mathbf{P}_t \mathbf{u}] - \eta_t w_d (\mathbf{D} \theta_t)^\top \mathbf{u} \\ &+ \frac{1}{2} \eta_t^2 \mathbb{E}[\Delta\theta_t^\top \mathbf{H}_{\text{eval}}(\Theta_t) \Delta\theta_t] \\ &+ \frac{L_H}{6} \eta_t^3 \mathbb{E}[\|\Delta\theta_t\|^3], \end{aligned}$$

Moreover, if under  $\rho$ -smoothness, Eq. (15) yields

$$\begin{aligned} \mathbb{E}[\Delta\mathcal{L}_{\text{eval}}] &\leq -\eta_t \mathbb{E}[(\mathbf{P}_t \hat{m}_t)^\top \mathbf{u}] \\ &- \eta_t w_d (\mathbf{D} \theta_t)^\top \mathbf{u} \\ &+ \frac{\rho}{2} \eta_t^2 \mathbb{E}[\|\Delta\theta_t\|^2]. \end{aligned}$$

In both cases the alignment term becomes  $\mathbb{E}[(\mathbf{P}_t \hat{m}_t)^\top \mathbf{u}]$ , which is in line with SDG in the main content of this paper.

## B.2. Proxy Alignment in Subspace

In this section, we prove Theorem 1 and state two practical corollaries.

In the end-point subspace let  $\mathbf{g} = \mathbf{g}_\vartheta(z)$ ,  $\boldsymbol{\mu} = \mathbb{E}[\mathbf{g}]$ ,  $\mathbf{g}_c = \mathbf{g} - \boldsymbol{\mu}$ , and  $\Sigma_g = \text{Cov}[\mathbf{g}] \succeq 0$ . Locally,

$$\nabla_\theta \ell(z) = \mathbf{J} \mathbf{g} + \mathbf{r}(z), \quad \mathbf{u} = \bar{\mathbf{J}} \mathbf{u}_\vartheta + \boldsymbol{\varepsilon},$$

with  $\mathbf{J}, \bar{\mathbf{J}}$  linear maps, residual  $\mathbf{r}(z)$ , and deterministic mismatch  $\boldsymbol{\varepsilon}$ . Define

$$\mathbf{S} = \frac{1}{2} (\mathbf{J}^\top \bar{\mathbf{J}} + \bar{\mathbf{J}}^\top \mathbf{J}), \quad \mathbf{A} = \frac{1}{2} (\mathbf{J}^\top \bar{\mathbf{J}} - \bar{\mathbf{J}}^\top \mathbf{J}),$$

and consider

$$X(z) = \mathbf{u}_\vartheta^\top \mathbf{g}_c, \quad Y(z) = (\nabla_\theta \ell(z))^\top \mathbf{u}.$$

Collect the remaining random terms into

$$\zeta(z) = (\mathbf{J} \mathbf{g}_c)^\top \boldsymbol{\varepsilon} + \mathbf{r}(z)^\top \bar{\mathbf{J}} \mathbf{u}_\vartheta + \mathbf{r}(z)^\top \boldsymbol{\varepsilon} + \mathbf{g}_c^\top \mathbf{A} \mathbf{u}_\vartheta,$$

and write  $\sigma_\zeta^2 = \text{Var}[\zeta(z)]$ .

**Proof of Theorem 1.** Let  $\tilde{\mathbf{g}} = \Sigma_g^{-1/2} \mathbf{g}_c$ ,  $\alpha = \Sigma_g^{1/2} \mathbf{u}_\vartheta$ ,  $B = \Sigma_g^{1/2} \mathbf{S} \Sigma_g^{-1/2}$ , and  $Z(z) = \mathbf{g}_c^\top \mathbf{S} \mathbf{u}_\vartheta = \alpha^\top B \tilde{\mathbf{g}}$ . If  $\zeta$  is uncorrelated with  $\tilde{\mathbf{g}}$  then  $\text{Cov}(X, Y) = \text{Cov}(X, Z)$  and  $\text{Var}(Y) = \text{Var}(Z) + \sigma_\zeta^2$ . Using

$$\begin{aligned} \text{Var}(X) &= \|\alpha\|_2^2, \\ \text{Cov}(X, Z) &= \alpha^\top \text{sym}(B) \alpha, \\ \text{Var}(Z) &\leq \|B\|_2^2 \|\alpha\|_2^2. \end{aligned}$$

and the Rayleigh-Ritz principle, gives

$$\rho_{XY} \geq \frac{\lambda_{\min}(\text{sym}(B))}{\sqrt{\|B\|_2^2 + \sigma_\zeta^2 / (\mathbf{u}_\vartheta^\top \Sigma_\vartheta \mathbf{u}_\vartheta)}}, \quad (17)$$

which is Eq. (6) in the main content after identifying  $B$ . Without the uncorrelatedness assumption, Cauchy-Schwarz implies the fallback bound

$$\rho_{XY} \geq \frac{\lambda_{\min}(\text{sym}(B)) \|\alpha\|_2 - \sigma_\zeta}{\|B\|_2 \|\alpha\|_2 + \sigma_\zeta}. \quad (18)$$

### B.3. Negative Pair Curvature

In the projection-temperature subspace, we write  $\mathbf{g}(z) = \mathbf{g}_\vartheta(z)$  and  $\mathbf{u} = \mathbf{u}_\vartheta$ . For softmax-type losses, a generalized Gauss-Newton curvature admits the population decomposition

$$\begin{aligned} \mathbf{H}_\vartheta &= \Phi_{\text{pos}} + \Phi_{\text{neg}}, \\ \Phi_{\text{pos}} &= \mathbb{E}_z[\mathbf{g}(z)\mathbf{g}(z)^\top], \\ \Phi_{\text{neg}} &= \mathbb{E}_{z \neq z'}[\mathbf{g}(z)\mathbf{g}(z')^\top], \end{aligned} \quad (19)$$

which mirrors the random-negative mechanism of InfoNCE. Note that  $\Phi_{\text{pos}} \succeq 0$  while  $\Phi_{\text{neg}}$  need not be PSD, and the sum  $\mathbf{H}_\vartheta$  is PSD.

For a mini-batch  $\{z_i\}_{i=1}^B$  let  $\mathbf{g}_i = \mathbf{g}_\vartheta(z_i)$ , then

$$\hat{\Phi}_{\text{pos}} = \frac{1}{B} \sum_{i=1}^B \mathbf{g}_i \mathbf{g}_i^\top, \quad \hat{\Phi}_{\text{neg}} = \frac{1}{B(B-1)} \sum_{i \neq j} \mathbf{g}_i \mathbf{g}_j^\top. \quad (20)$$

As in Eq. (8), define

$$\mathbf{H}_\vartheta^{(\alpha)} = (1-\alpha) \Phi_{\text{pos}} + \alpha \Phi_{\text{neg}}, \quad \mathbf{M} = \mathbf{H}_\vartheta^{(\alpha)} + \lambda \mathbf{I}, \quad (21)$$

with  $\alpha \in [0, 1]$  and  $\lambda > 0$ . Let  $A^*(z) = \mathbf{g}(z)^\top \mathbf{H}_\vartheta^{-1} \mathbf{u}$ ,  $A_\alpha(z) = \mathbf{g}(z)^\top \mathbf{M}^{-1} \mathbf{u}$ , and  $\Delta_\alpha = \mathbf{H}_\vartheta - \mathbf{H}_\vartheta^{(\alpha)}$ . Using the resolvent identity,

$$\begin{aligned} \mathbf{M}^{-1} - \mathbf{H}_\vartheta^{-1} &= \mathbf{H}_\vartheta^{-1} (\Delta_\alpha - \lambda \mathbf{I}) \mathbf{M}^{-1}, \\ \|\mathbf{M}^{-1} - \mathbf{H}_\vartheta^{-1}\|_2 &\leq \|\mathbf{H}_\vartheta^{-1}\|_2 \|\Delta_\alpha\|_2 \|\mathbf{M}^{-1}\|_2. \end{aligned} \quad (22)$$

which leads to

$$\mathbb{E}_z[(A_\alpha - A^*)^2] \leq C_2 \|\Delta_\alpha\|_F^2 \|\mathbf{H}_\vartheta^{-1} \mathbf{u}\|_2^2,$$

for a constant  $C_2 > 0$  depending only on  $\|\Phi_{\text{pos}}\|_2$ ,  $\|\mathbf{H}_\vartheta^{-1}\|_2$ , and  $\|\mathbf{M}^{-1}\|_2$ . Whenever cross-example coupling is present, any  $\alpha > 0$  that injects off-diagonal mass reduces  $\|\Delta_\alpha\|_F$ . Let  $\Pi_k \in \mathbb{R}^{k \times d_\vartheta}$  be a JL transform. For any fixed  $\mathbf{a}, \mathbf{b}$ ,  $|\mathbf{a}^\top \mathbf{b} - (\Pi_k \mathbf{a})^\top (\Pi_k \mathbf{b})| \leq \varepsilon \|\mathbf{a}\| \|\mathbf{b}\|$  holds with probability at least  $1 - \delta$ , where  $k = \Omega(\varepsilon^{-2} \log(1/\delta))$ . Define  $\mathbf{M}_k = \Pi_k \mathbf{M} \Pi_k^\top$  and  $\tilde{\mathbf{u}}_k = \mathbf{M}_k^{-1} \Pi_k \mathbf{u}$ . The sketched score

$$\hat{A}_\alpha(z) = (\Pi_k \mathbf{g}(z))^\top \tilde{\mathbf{u}}_k$$

satisfies  $\mathbb{E}_z[(\hat{A}_\alpha - A_\alpha)^2] \leq C_1 \log(1/\delta)/k$  for a constant  $C_1 > 0$  depending on  $\|\mathbf{M}^{-1}\|_2$ ,  $\|\mathbf{u}\|_2$ , and  $\mathbb{E}\|\mathbf{g}(z)\|_2^2$ . Combining with the mixing bias via the triangle inequality yields Eq. (9) in the main content:

$$\begin{aligned} \mathbb{E}_z[(\hat{A}_\alpha(z) - A^*(z))^2] &\leq \underbrace{\frac{C_1 \log(1/\delta)}{k}}_{\text{projection variance}} \\ &\quad + \underbrace{C_2 \|\Delta_\alpha\|_F^2 \|\mathbf{H}_\vartheta^{-1} \mathbf{u}_\vartheta\|_2^2}_{\text{curvature bias}}. \end{aligned} \quad (23)$$

## C. Data Selection Implementation Details

This section provides all components needed to reproduce CHIPS and baseline methods.

### C.1. Problem Setup

Let the training pool be  $\mathcal{D}_{\text{pool}} = \{(x_i, y_i)\}_{i=1}^N$  and the evaluation set be  $\mathcal{D}_{\text{eval}} = \{(x_m, y_m)\}_{m=1}^M$ . Given a data retention ratio  $r \in (0, 1]$ , we select  $n = \lfloor r \times |\mathcal{D}_{\text{pool}}| \rfloor$  samples from  $\mathcal{D}_{\text{pool}}$  to perform CPT. CHIPS operates in CLIP’s end-point subspace  $\vartheta = \{\mathbf{W}_v, \mathbf{W}_t, \tau\}$  where  $\mathbf{W}_v$  and  $\mathbf{W}_t$  are the projection heads for vision and text, and  $\tau > 0$  is the logit scale. For computational efficiency, backbone encoders are used to produce features and are kept fixed for computing selection utility scores (we only need training dynamics of  $\vartheta$  instead of the complete model).

Let  $\mathbf{h} = \text{CLIP}_{\text{img}}(x)$  and  $\mathbf{t} = \text{CLIP}_{\text{txt}}(y)$  be backbone features. Define L2-normalized end-point embeddings

$$\hat{\mathbf{x}} = \frac{\mathbf{W}_v \mathbf{h}}{\|\mathbf{W}_v \mathbf{h}\|}, \quad \hat{\mathbf{y}} = \frac{\mathbf{W}_t \mathbf{t}}{\|\mathbf{W}_t \mathbf{t}\|},$$

and similarities  $s_{ij} = \tau \hat{\mathbf{x}}_i^\top \hat{\mathbf{y}}_j$ . For a batch of size  $B$ , write  $\mathbf{S} = [s_{ij}]_{i,j=1}^B$  and define the bidirectional softmax probabilities

$$p_{ij}^{i2t} = \frac{\exp(s_{ij})}{\sum_{j'} \exp(s_{ij'})}, \quad p_{ij}^{t2i} = \frac{\exp(s_{ij})}{\sum_{i'} \exp(s_{i'j})}.$$

The symmetric InfoNCE loss for sample  $i$  is

$$\ell_i(\vartheta) = \frac{1}{2} (\text{CE}(\mathbf{S}_{i,:}, i) + \text{CE}(\mathbf{S}_{:,i}, i)),$$

where CE denotes the cross-entropy loss.

Let  $\mathbf{g}_\vartheta(z) = \nabla_\vartheta \ell(z; \vartheta) \in \mathbb{R}^d$  denote the end-point gradient of a sample, and let

$$\mathbf{u}_\vartheta \triangleq \mathbb{E}_{z \sim \mathcal{D}_{\text{eval}}}[\mathbf{g}_\vartheta(z)]$$

be the evaluation mean gradient in the same subspace. In practice we maintain  $\mathbf{u}_\vartheta$  by an exponential moving average over random evaluation minibatches.

Moreover, to reduce computational cost we use a JL map matrix  $\Pi_k \in \mathbb{R}^{k \times d}$  and work with sketched vectors

$\mathbf{g}_k = \Pi_k \mathbf{g}_\vartheta$  and  $\mathbf{u}_k = \Pi_k \mathbf{u}_\vartheta$ . The inner product distortion satisfies  $|\mathbf{a}^\top \mathbf{b} - (\Pi_k \mathbf{a})^\top (\Pi_k \mathbf{b})| \leq \varepsilon \|\mathbf{a}\| \|\mathbf{b}\|$  with probability at least  $1 - \delta$  when  $k = \Omega(\varepsilon^{-2} \log(1/\delta))$ , which is also used in App. B.3.

## C.2. CHIPS

CHIPS ranks each  $z \in \mathcal{D}_{\text{pool}}$  by the multiplicative utility

$$\mathcal{I}_{\text{CHIPS}}(z) = \widehat{A}_\alpha(z) \cdot w_L(z) \cdot w_R(z),$$

then selects the top  $n$  samples for CPT. The three factors are implemented as follows and the complete process of CHIPS is provided in Alg. 1.

**Curvature-aware proxy alignment.** We estimate the curvature in  $\vartheta$  by mixing self and cross moments from symmetric InfoNCE, consistent with Sec. 2.3. Maintain EMA estimators

$$\Phi_{\text{pos}} = \mathbb{E}[\mathbf{g}_\vartheta(z) \mathbf{g}_\vartheta(z)^\top], \quad \Phi_{\text{neg}} = \mathbb{E}_{z \neq z'}[\mathbf{g}_\vartheta(z) \mathbf{g}_\vartheta(z')^\top],$$

then build

$$\mathbf{M} = \mathbf{H}_\vartheta^{(\alpha)} + \lambda \mathbf{I}, \quad \mathbf{H}_\vartheta^{(\alpha)} = (1 - \alpha) \Phi_{\text{pos}} + \alpha \Phi_{\text{neg}},$$

with  $\alpha \in [0, 1]$  and ridge  $\lambda > 0$ . Without sketching, the alignment score is

$$A_\alpha(z) = \mathbf{g}_\vartheta(z)^\top \mathbf{M}^{-1} \mathbf{u}_\vartheta.$$

With a JL sketch, form  $\mathbf{M}_k = \Pi_k \mathbf{M} \Pi_k^\top$  once per update and solve  $\bar{\mathbf{u}}_k = \mathbf{M}_k^{-1} \mathbf{u}_k$ . The sketched score is

$$\widehat{A}_\alpha(z) = (\Pi_k \mathbf{g}_\vartheta(z))^\top \bar{\mathbf{u}}_k.$$

This matches Eq. (4) and App. B.3.

**Learnability.** Compute correctness and hardest negative margin using the current batch statistics

$$\begin{aligned} p_{\text{corr}}(z) &= \frac{1}{2} (p_{ii}^{i2t} + p_{ii}^{t2i}), \\ m(z) &= s_{ii} - \max_{j \neq i} \{s_{ij}\}, \max_{i' \neq i} \{s_{i'i}\}. \end{aligned} \quad (24)$$

Define the learnability weight as in Eq. (11)

$$w_L(z) = (1 - p_{\text{corr}}(z)) (1 + \sigma(-m(z))),$$

which upweights near-boundary samples and downweights saturated ones.

**Target-domain relevance.** Let the evaluation centroids be  $\boldsymbol{\mu}_x = \mathbb{E}[\hat{\mathbf{x}}]$  and  $\boldsymbol{\mu}_y = \mathbb{E}[\hat{\mathbf{y}}]$  over  $\mathcal{D}_{\text{eval}}$ . Following Eq. (12),

$$w_R(z) = \sigma\left((1 - \beta) \cos(\hat{\mathbf{x}}, \boldsymbol{\mu}_x) + \beta \cos(\hat{\mathbf{y}}, \boldsymbol{\mu}_y)\right),$$

which softly reweights toward the evaluation domain while keeping the selection drift bounded.

---

## Algorithm 1 CHIPS Algorithm

---

**Require:** pool  $\mathcal{D}_{\text{pool}}$ , evaluation set  $\mathcal{D}_{\text{eval}}$ , retention  $n$ , mix  $\alpha$ , ridge  $\lambda$ , JL dim  $k$ , relevance balance  $\beta$

- 1: Estimate  $\mathbf{u}_\vartheta \leftarrow \mathbb{E}_{z \sim \mathcal{D}_{\text{eval}}}[\mathbf{g}_\vartheta(z)]$  using minibatches; cache  $\boldsymbol{\mu}_x, \boldsymbol{\mu}_y$
- 2: Initialize EMA moments  $\Phi_{\text{pos}} \leftarrow \mathbf{0}, \Phi_{\text{neg}} \leftarrow \mathbf{0}$
- 3: **for** each minibatch  $\{z_i\}_{i=1}^B$  sampled from  $\mathcal{D}_{\text{pool}}$  **do**
- 4:   compute  $\mathbf{g}_i = \mathbf{g}_\vartheta(z_i)$  for all  $i$
- 5:   update  $\Phi_{\text{pos}}$  and  $\Phi_{\text{neg}}$  using the batch  $U$ -statistics and EMA
- 6: **end for**
- 7:  $\mathbf{M} \leftarrow (1 - \alpha) \Phi_{\text{pos}} + \alpha \Phi_{\text{neg}} + \lambda \mathbf{I}$
- 8: **if**  $k > 0$  **then**
- 9:   sample JL  $\Pi_k$ , set  $\mathbf{M}_k = \Pi_k \mathbf{M} \Pi_k^\top$ , solve  $\bar{\mathbf{u}}_k = \mathbf{M}_k^{-1} (\Pi_k \mathbf{u}_\vartheta)$
- 10: **end if**
- 11: **for** each  $z = (x, y) \in \mathcal{D}_{\text{pool}}$  **do**
- 12:   compute  $\mathbf{g} = \mathbf{g}_\vartheta(z)$  and  $\widehat{A}_\alpha(z) = \begin{cases} \mathbf{g}^\top \mathbf{M}^{-1} \mathbf{u}_\vartheta, & k = 0 \\ (\Pi_k \mathbf{g})^\top \bar{\mathbf{u}}_k, & k > 0 \end{cases}$
- 13:   compute  $p_{\text{corr}}(z)$  and  $m(z)$ , then  $w_L(z) = (1 - p_{\text{corr}}(z)) (1 + \sigma(-m(z)))$
- 14:   compute  $w_R(z) = \sigma((1 - \beta) \cos(\hat{\mathbf{x}}, \boldsymbol{\mu}_x) + \beta \cos(\hat{\mathbf{y}}, \boldsymbol{\mu}_y))$
- 15:   set  $\mathcal{I}_{\text{CHIPS}}(z) = \widehat{A}_\alpha(z) w_L(z) w_R(z)$
- 16: **end for**
- 17: return the top  $n$  samples by  $\mathcal{I}_{\text{CHIPS}}$

---

**More details.** During the computation process,

- $\mathbf{M}^{-1} \mathbf{u}_\vartheta$  is reused across all samples, so the per-sample cost is dominated by  $\mathbf{g}_\vartheta(z)$  and a dot product in  $d$  or  $k$  dimensions.
- $\tau$  is kept positive by parameterizing  $\tau = \exp(\tilde{\tau})$ .
- We rescale  $\mathcal{I}_{\text{CHIPS}}$  within each shard of  $\mathcal{D}_{\text{pool}}$  if memory constraints require sharded processing.
- We recompute  $\mathbf{u}_\vartheta$  periodically to track drift during CPT.

## C.3. Heuristics-based Baselines

All heuristics select the top  $n$  samples under their scores.

- **Random** samples uniformly at random without replacement.
- **CLIPScore** ranks by CLIPScore [21] computed with the frozen base CLIP model.
- **Concept-Balance** performs probabilistic downsampling to flatten concept frequency. Following [36], we down-sample overrepresented concepts such as *Plots and Charts, Tables, and Scientific Formulae and Equations* at rate 0.25, then sample the remainder uniformly.
- **Concept-Filter** keeps only samples whose metadata contain any of the eight whitelist concepts in [36], (*Clinical Imaging, Microscopy, Immuno Assays, Illustrative Dia-*

grams, Chemical Structures, Maps, Tools and Materials, and Hand Drawn and Screen Based Visuals) then samples uniformly from the filtered pool.

#### C.4. Influence-based Baselines in the End-point Subspace

For fairness and to avoid conflicts with the main text, all influence baselines use the same end-point gradients  $\mathbf{g}_\vartheta$  and the same optional JL sketch  $\Pi_k$  as CHIPS. Let  $\tilde{\mathbf{g}}_i = \Pi_k \mathbf{g}_\vartheta(z_i)$  if  $k > 0$  (use  $\tilde{\mathbf{g}}_i = \mathbf{g}_\vartheta(z_i)$  when  $k = 0$ ). Let the evaluation mean gradient be  $\bar{\mathbf{g}}_{\text{eval}} = \frac{1}{M} \sum_{m=1}^M \tilde{\mathbf{g}}_m^{\text{eval}}$ .

**Dot [67].** The first-order directional alignment is

$$\mathcal{I}_{\text{Dot}}(i) = \tilde{\mathbf{g}}_i^\top \bar{\mathbf{g}}_{\text{eval}}.$$

**TracIn [43].** Given checkpoints  $\{\theta_t\}_{t=0}^{T-1}$  and learning rates  $\{\eta_t\}$ , we accumulate

$$\mathcal{I}_{\text{TracIn}}(i) = \sum_{t=0}^{T-1} \eta_t (\tilde{\mathbf{g}}_i^{(t)})^\top \bar{\mathbf{g}}_{\text{eval}},$$

where  $\tilde{\mathbf{g}}_i^{(t)} = \Pi_k \nabla_{\vartheta} \ell_i(\theta_t)$ . We keep  $\bar{\mathbf{g}}_{\text{eval}}$  fixed for computational stability.

**TRAK [40].** We form a regularized second-moment matrix in the same feature space

$$\Phi = \frac{1}{N} \sum_{i=1}^N \tilde{\mathbf{g}}_i \tilde{\mathbf{g}}_i^\top + \lambda_{\text{TRAK}} \mathbf{I},$$

and compute

$$\mathcal{I}_{\text{TRAK}}(i) = \tilde{\mathbf{g}}_i^\top \Phi^{-1} \bar{\mathbf{g}}_{\text{eval}}.$$

**CHIPS for comparison.** CHIPS differs from Dot and TRAK by preconditioning with  $\mathbf{M}$  that mixes  $\Phi_{\text{pos}}$  and  $\Phi_{\text{neg}}$  as in Sec. C.2, and by multiplying learnability and relevance weights. In the sketched space,

$$\mathcal{I}_{\text{CHIPS}}(i) = (\tilde{\mathbf{g}}_i^\top \mathbf{M}_k^{-1} \mathbf{u}_k) w_L(i) w_R(i),$$

where  $\mathbf{M}_k = \Pi_k ((1 - \alpha)\Phi_{\text{pos}} + \alpha\Phi_{\text{neg}} + \lambda \mathbf{I}) \Pi_k^\top$ .

#### D. Score Distribution

The score distributions of CLIPScore, Dot, TracIn, TRAK, and CHIPS are provided in Fig. 5, Fig. 6, Fig. 7, Fig. 8, and Fig. 9.

## E. Training

### E.1. Software and Distributed Setup

**Framework and precision.** We train with PyTorch in distributed data-parallel mode. On H200 GPUs we use bfloat16 for tensor computation with an fp32 master copy of parameters for the AdamW states. The logit-scale parameter is maintained as  $\tilde{\tau} \in \mathbb{R}$  and realized at runtime by  $\tau = \exp(\tilde{\tau})$  to guarantee positivity. Softmax and cross-entropy are evaluated with numerically stable log-sum-exp.

**Communication.** Gradients are synchronized by NCCL with bucket size tuned to saturate NVLink. We enable gradient accumulation when the per-GPU micro-batch would otherwise exceed memory budget. Let  $G$  be the number of GPUs,  $B_{\text{micro}}$  the per-GPU micro-batch, and  $A$  the accumulation steps, then the global batch is

$$B_{\text{global}} = G \times B_{\text{micro}} \times A.$$

We choose  $G = 8$ ,  $B_{\text{micro}} = 4096$  and  $A = 1$  such that  $B_{\text{global}} = 32,768$  as in the main content.

**Determinism.** We fix seeds for Python, NumPy, and CUDA RNGs and set cuDNN to deterministic kernels where available. Dataset sharding and sampler seeds are logged per epoch to make re-runs bitwise reproducible up to nondeterminism in fused kernels.

### E.2. Data Preprocessing and Batching

**Image pipeline.** Training images are decoded to RGB and resized to the default input resolution of each MetaCLIP variant. We apply random resized crop that preserves aspect ratio, followed by horizontal flip with probability 0.5. Pixel intensities are normalized by CLIP mean and variance. Center crop is used at evaluation time.

**Text pipeline.** Texts are normalized by Unicode and then tokenized by the CLIP tokenizer. Sequences are truncated to the CLIP maximum length (77 tokens) with special tokens preserved.

**Sharding and streaming.** The training pools are sharded into balanced files on disk to avoid hot spots. Each worker maintains a streaming iterator with prefetching in pinned memory. We keep sharding consistent across methods so that all runs process the same examples at the same step counts.

### E.3. Optimization Schedule

**Optimizer and parameter groups.** We use AdamW with  $(\beta_1, \beta_2, \epsilon) = (0.9, 0.98, 10^{-6})$  as stated in the main text. Weight decay is applied to all trainable parameters except LayerNorm and bias parameters.

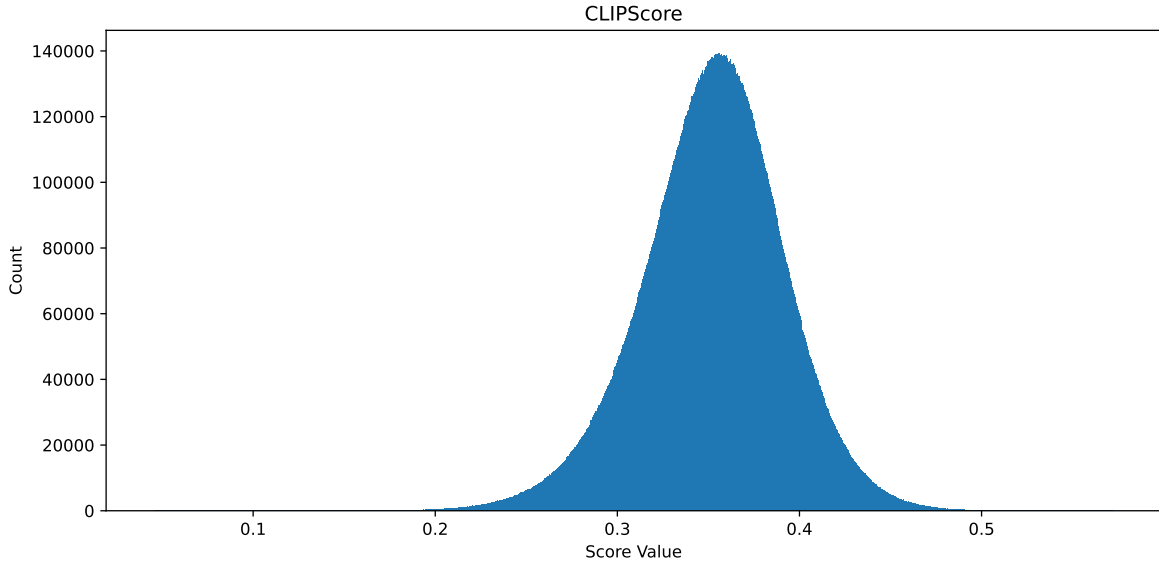


Figure 5. Distribution of CLIPScore on BIOMEDICA.

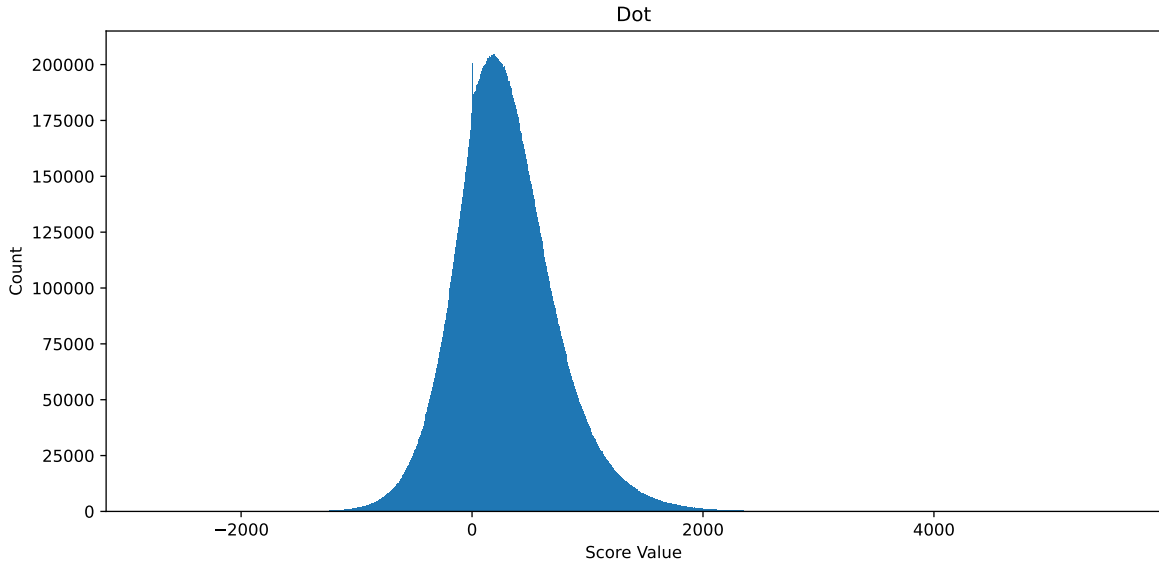


Figure 6. Distribution of Dot on BIOMEDICA.

**Learning-rate scheduler.** We use a cosine decay scheduler over the total number of optimizer steps. Unless specified otherwise, the peak learning rate equals the initial value  $10^{-6}$ . We optionally use a short linear warmup of  $T_{\text{warm}}$  steps when training with heavier augmentation or larger  $B_{\text{global}}$ . The final learning rate floor is set to 0 unless explicit floor is reported.

#### E.4. Counting Steps and Budget Fairness

Let  $n = \lfloor r \times |\mathcal{D}_{\text{train}}| \rfloor$  be the number of retained samples,  $E$  the number of epochs, and  $B_{\text{global}}$  the global batch size. The number of optimizer steps per run is

$$T_{\text{steps}} = \left\lceil \frac{n}{B_{\text{global}}} \right\rceil \times E.$$

All methods, including baselines and CHIPS, are trained for the same  $T_{\text{steps}}$ . The wall-clock overhead of selection

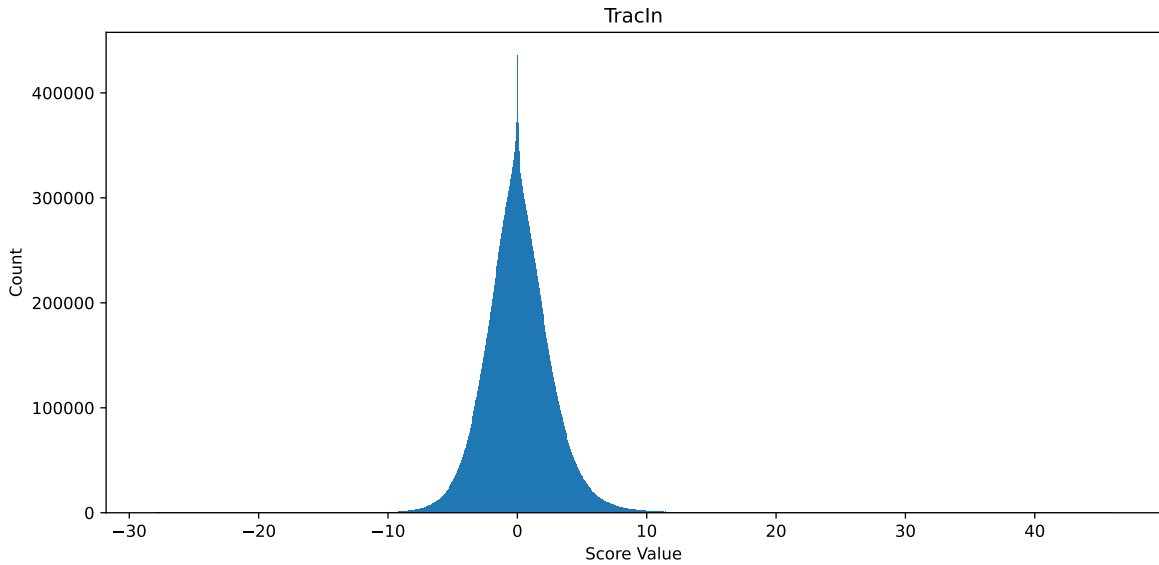


Figure 7. Distribution of TracIn on BIOMEDICA.

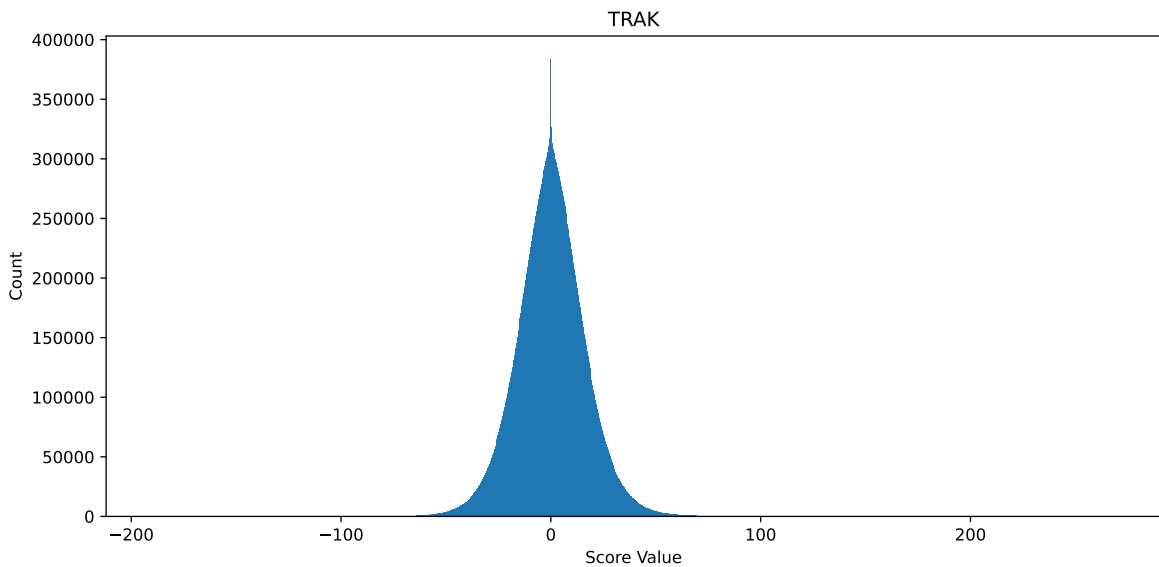


Figure 8. Distribution of TRAK on BIOMEDICA.

is measured separately and reported as a percentage of the total training time.

## F. Evaluation

To ensure a comprehensive and reproducible evaluation, we include 48 datasets covering both general-domain and medical-domain visual understanding tasks for this paper. Detailed descriptions are provided below.

### F.1. General-Domain Datasets

For General-Domain Datasets, they span a variety of recognition and retrieval tasks, including classification, fine-grained categorization, visual reasoning, robustness evaluation, and multimodal understanding. To be specific, we give an overall description for each as follows:

#### Object & Scene Classification:

- **ImageNet-1K** [8]: A large-scale object classification benchmark with 1.28 million training images and 1,000

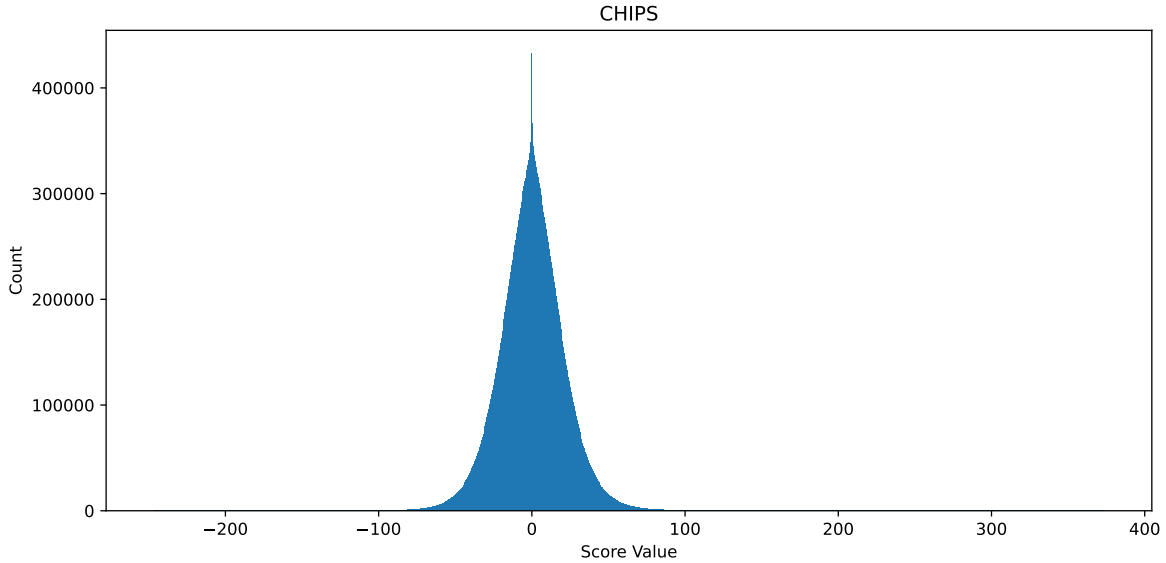


Figure 9. Distribution of CHIPS on BIOMEDICA.

object categories, widely used as a baseline in deep vision.

- **ImageNetV2** [45]: A re-collected test set for ImageNet, designed to assess generalisation under dataset shift for the same 1,000 categories.
- **SUN397** [55]: A scene recognition dataset containing 397 scene categories of diverse indoor/outdoor types, enabling evaluation on scene-level classification.
- **Caltech-101** [13]: A mid-scale object classification benchmark with 101 categories and around 9,000 images, used historically for transfer-learning studies.
- **VOC2007** [12]: The PASCAL Visual Object Classes 2007 dataset, including object classification (and detection) tasks across 20 categories in real-world scenes.

#### Fine-Grained Recognition:

- **Cars** [29]: A fine-grained vehicle classification dataset containing many car make/model/year classes, evaluating subtle visual differences among similar objects.
- **Aircraft** [37]: A fine-grained aircraft dataset distinguishing among many aircraft models and variants, used for high-granularity recognition research.
- **Food101** [3]: A food image dataset covering 101 food types, with 101,000 images total, for fine-grained categorisation of dishes.
- **Oxford Flowers (Flowers102)** [39]: A flower species classification dataset with 102 categories and 8,000 images, common in fine-grained vision tasks.
- **Pets** [41]: A fine-grained pet breed classification dataset (cats & dogs) with multiple breeds and varied poses/backgrounds.

#### Texture, Shape, Small-Scale Objects:

- **CIFAR-10/100** [30]: Standard small-scale image classification datasets with 10 (CIFAR-10) and 100 (CIFAR-100) classes, each containing 60,000 colour images of 32×32 size.
- **MNIST** [31]: Classic handwritten digit classification dataset with 70,000 grayscale images of digits 0-9, often used for benchmarking basic vision models.
- **STL-10** [7]: A dataset derived from ImageNet with 10 classes and high-resolution images, used for unsupervised / transfer learning in small-scale settings.
- **smallNORB (Azimuth/Elevation)** [32]: A synthetic 3D object dataset capturing objects under different view-points (azimuth/elevation), for studying pose-invariance and representation robustness.
- **SVHN** [38]: Street View House Numbers dataset with real-world digital number images, used for digit recognition in situ.

#### Robustness & Out-of-Distribution:

- **ImageNet-A** [20]: A subset of ImageNet containing “adversarially filtered” images challenging standard models, designed to test worst-case object recognition robustness.
- **ImageNet-O** [20]: An out-of-distribution test set for ImageNet models, containing images from unknown classes not present in training, to measure OOD detection/generalisation.

#### Domain-Specific Recognition:

- **KITTI** [14]: A dataset collected for autonomous driving, including object, scene and motion tasks—here used in the classification context of road-scene recognition.
- **EuroSAT** [19]: A remote sensing image classification dataset with 45 scene types, aimed at land-use and

satellite-image recognition.

- **RESISC45** [5]: Another remote sensing scene classification dataset covering 45 classes of aerial images, evaluating models on high-altitude imagery.

#### Visual Reasoning & Synthetic Tasks:

- **CLEVR (Closest-Object-Distance / Count-All)** [26]: A synthetic benchmark for visual reasoning, where models answer compositional questions about objects (distance/count) in rendered scenes.
- **DTD** [6]: The Describable Texture Dataset, focusing on texture/material recognition with diverse patterns, supporting generalisation in less object-centric tasks.

#### Image-Text Retrieval / Multimodal:

- **Flickr8k** [22]: An image-caption dataset with 8,000 images, used for evaluating image-to-text and text-to-image retrieval and captioning systems.
- **Flickr30k** [63]: A larger image-caption dataset with 30,000 images, used widely in cross-modal retrieval research.
- **MSCOCO** [33]: A large-scale multimodal dataset with 120K+ images and captions, supporting image detection, segmentation and retrieval tasks.
- **Rendered-SST2** [44]: A dataset created by rendering the sentences from the Stanford Sentiment Treebank v2 into images (positive/negative labels), used to assess optical-character-recognition via image encoders. (Train: 6,920 images; Val: 872; Test: 1,821).

#### Geographic / Landmark Classification:

- **Country211** [44]: A dataset designed for geolocation classification, filtered from the YFCC100M dataset—211 countries/territories, with 150 train / 50 val / 100 test images per country.

## F.2. Medical-Domain Datasets

For Medical-Domain Datasets, we include a broad range of imaging modalities and clinical specialties, covering ophthalmology, radiology, dermatology, hematology, pathology, neuropathology, and non-clinical biology. These datasets collectively assess model performance in clinically relevant scenarios and diagnostic contexts. From a task perspective, they can be broadly grouped into three major categories: *disease classification*, *organ and tissue recognition*, and *pathological image analysis*, with an additional category for *non-clinical biological imaging*. Together, they form a comprehensive benchmark for evaluating generalization and robustness of visual models in biomedical applications. In detail, the brief introduction of included datasets are listed:

#### Disease Classification:

- **Diabetic Retinopathy** [11]: A fundus-image dataset for grading diabetic retinopathy severity in ophthalmology, used for multi-class disease classification.
- **RetinaMNIST / OCTMNIST** [61]: Retinal fundus and

optical coherence tomography (OCT) image datasets for ophthalmic disease classification across multiple categories; part of the MedMNIST benchmark (about 708k 2D images in total for the MedMNIST collection).

- **ChestMNIST** [61]: Based on the NIH-ChestXray14 dataset, ChestMNIST contains 112,120 chest X-ray images, formulated as a multi-label classification task for detecting 14 different diseases.
- **ChestX-ray14** [52]: A large collection of over 100,000 frontal-view chest X-ray images from more than 30,000 patients. The labels for eight common thoracic diseases were automatically generated by text-mining the associated radiological reports.
- **DermaMNIST** [61]: This is a multi-class classification dataset of 10,015 dermatoscopic images for identifying 7 different types of common pigmented skin lesions.
- **BloodMNIST** [61]: A hematology microscope-image dataset containing 17,092 images across 8 classes, used for blood-cell type classification.

#### Organ and Tissue Recognition:

- **OrganAMNIST / OrganCMNIST / OrganSMNIST** [61]: This dataset is for multi-class classification of 11 body organs, containing 58,850 images derived from axial-view slices of abdominal CT scans and resized to 28x28 pixels.
- **TissueMNIST** [61]: Sourced from the Broad Bioimage Benchmark Collection, TissueMNIST is a large-scale dataset of 236,386 human kidney cortex cells, organized into 8 categories for a multi-class classification task.

#### Pathological Image Analysis:

- **PCAM** [51]: The dataset is a large-scale collection of 96x96 pixel histopathology image patches extracted from the Camelyon16 challenge, designed for the task of identifying metastatic cancer in lymph node sections.
- **LC25000** [2]: The LC25000 dataset contains 25,000 color histopathological images across five classes, featuring both cancerous and benign tissues from the lung and colon.
- **PathMNIST** [61]: PathMNIST is a multi-class classification dataset derived from colorectal cancer histology slides. It is comprised of 107,180 image patches, categorized into 9 distinct tissue types.
- **Amyloid CAA/Diffuse** [53]: It includes 100495 annotations on 20099 candidate amyloid beta neuropathologies, which is a neuropathology image dataset for subtypes of amyloid pathology in brain tissue, used for subtype classification tasks.

#### Non-Clinical Biological Imaging:

- **Pollen** [1]: The Pollen13K dataset is a large-scale collection of over 13,000 microscopic pollen grain images from aerobiological samples, used for biological particle classification. It was chosen to test model generalization on complex, non-clinical imagery.

## G. FLOPs Computation

This appendix consolidates the FLOPs counting procedure for BIOMEDICA [36] used to report scoring cost.

All totals below measure a single complete *scoring* pass over  $\mathcal{D}_{\text{train}}$  and use the batch primitives in Tab. 5:  $C_{\text{fwd}}(B)$ ,  $C_{\text{bwd}}(B)$ ,  $C_{\text{fb}}(B) = C_{\text{fwd}}(B) + C_{\text{bwd}}(B)$ , and  $C_{\text{jvp}}(B)$ . The random projection (CountSketch) cost per application is  $C_{\text{rp}} \approx 2P$  (see Sec. G). We denote  $n_{\text{train}} = \lceil N_{\text{train}}/B_{\text{train}} \rceil$  and  $n_{\text{eval}} = \lceil N_{\text{eval}}/B_{\text{eval}} \rceil$ . TracIn uses  $E$  epochs for accumulation. TRAK and CHIPS use  $I$  conjugate-gradient (CG) iterations.

**TracIn.** TracIn combines a single evaluation-direction construction with per-batch JVPs and trajectory accumulation:

$$C_{\text{TracIn}} = C_{\text{eval-dir}} + C_{\text{JVP-train}} + C_{\text{accum}}, \quad (25)$$

$$C_{\text{eval-dir}} = n_{\text{eval}} (C_{\text{fb}}(B_{\text{eval}}) + C_{\text{rp}}), \quad (26)$$

$$C_{\text{JVP-train}} = n_{\text{train}} C_{\text{jvp}}(B_{\text{train}}), \quad (27)$$

$$C_{\text{accum}} = E n_{\text{train}} C_{\text{fb}}(B_{\text{train}}). \quad (28)$$

**TRAK.** TRAK builds a second-order score with CG in the same end-point geometry. We write the shared backbone block once and reuse it:

$$\begin{aligned} \text{Base} &= n_{\text{eval}} (C_{\text{fb}}(B_{\text{eval}}) + C_{\text{rp}}) + C_{\text{proto-eval}} \\ &+ n_{\text{train}} (C_{\text{fb}}(B_{\text{train}}) + C_{\text{rp}}) \\ &+ I n_{\text{train}} (C_{\text{jvp}}(B_{\text{train}}) + C_{\text{fb}}(B_{\text{train}}) + C_{\text{rp}}) \\ &+ n_{\text{train}} (C_{\text{jvp}}(B_{\text{train}}) + C_{\text{fwd}}(B_{\text{train}})). \end{aligned} \quad (29)$$

The TRAK total is simply

$$C_{\text{TRAK}} = \text{Base}. \quad (30)$$

**CHIPS.** CHIPS shares Base with TRAK and adds three lightweight terms for (i) negative-pair curvature in the sketched space, (ii) hardest-negative margin bookkeeping, and (iii) two prototype similarities per batch for relevance. To avoid overlong lines we factor these contributions:

$$\Delta_{\text{neg}} \approx c_{\text{neg}} k \quad (31)$$

$$\Delta_{\text{margin}} \approx 2 B_{\text{train}}^2 \quad (32)$$

$$\Delta_{\text{rel}} \approx 4 B_{\text{train}} d \quad (33)$$

which are vector-level ops per CG iteration, hardest-negative search in a  $B_{\text{train}} \times B_{\text{train}}$  block, and two prototype similarities per batch.

The CHIPS total is then

$$\begin{aligned} C_{\text{CHIPS}} &= \text{Base} \\ &+ I \Delta_{\text{neg}} \\ &+ n_{\text{train}} \Delta_{\text{margin}} \\ &+ n_{\text{train}} \Delta_{\text{rel}}. \end{aligned} \quad (34)$$

$C_{\text{rp}}$  is incurred when forming the sketched evaluation direction and wherever sketched vectors are refreshed.  $\Delta_{\text{neg}}$  accounts for a handful of axpy-like operations per CG iteration in the  $k$ -dimensional sketched space.  $\Delta_{\text{margin}}$  is a max-reduction over off-diagonal logits already materialized for symmetric InfoNCE.  $\Delta_{\text{rel}}$  computes two dot products per sample with cached prototypes  $(\mu_x, \mu_y)$ .

### G.1. Numerical Totals

We instantiate Eqs. (25)–(34) with the fixed values above. We use  $E = 10$  epochs for TracIn and  $I = 5$  CG iterations for TRAK and CHIPS.

$$\text{TracIn } (E=10): \quad 5.258869 \times 10^{16}.$$

$$\text{TRAK } (I=5): \quad 5.094585 \times 10^{16}.$$

$$\text{CHIPS } (I=5): \quad 5.094747 \times 10^{16}.$$

### G.2. Assumptions and Further notes

- Symmetric CLIP computes logits in both directions;  $C_{\text{fwd}}(B)$  already includes the two  $B \times B$  matmuls in Eq. (5).
- The empirical bound  $C_{\text{jvp}}(B) \approx 2 C_{\text{fwd}}(B)$  holds for our implementation and batch shapes.
- The evaluation mean-gradient uses a single split with  $B_{\text{eval}} = 3400$ .  $C_{\text{proto-eval}}$  counts only projections and L2 norms.
- CountSketch is the default random projection; for other sketches replace  $C_{\text{rp}}$  with the appropriate cost model (sparse RP  $2sP$ , SRHT  $2m \log_2 m$ , dense Gaussian  $2kP$ ).
- FLOPs are operation counts independent of arithmetic precision and exclude file I/O and host preprocessing.
- *Scaling summary.* With fixed  $B$  and  $d$ , the dominant terms scale as  $\text{TracIn} = \Theta(E n_{\text{train}} C_{\text{fb}})$ ,  $\text{TRAK} = \Theta(I n_{\text{train}} C_{\text{fb}})$ ,  $\text{CHIPS} = \Theta(I n_{\text{train}} C_{\text{fb}}) + O(Ik + n_{\text{train}} B^2 + n_{\text{train}} B d)$ . At the reported  $k$  and  $B$ , the  $O(Ik)$  and  $O(n_{\text{train}} B d)$  extras are negligible and  $\Delta_{\text{margin}}$  is amortized by already-computed logits.

## H. Full Results

### H.1. Main Experiment

The full results of the main experiment are detailed in Tab. 6 and Tab. 7 for the medical domain, and in Tab. 8 through Tab. 11 for the general domain.

Quantity	Meaning	General formula	$B_{\text{train}}$	$B_{\text{eval}}$
$C_{\text{lin}}$	two linear projections to $d$	$2 B (d_v + d_t) d$	$4.294967296 \times 10^{10}$	$4.456448 \times 10^9$
$C_{\text{norm}}$	two L2 normalizations	$\approx 6 B d$	$1.00663296 \times 10^8$	$1.04448 \times 10^7$
$C_{\text{mm}}$	logits matmul for one direction	$2 B^2 d$	$1.099511627776 \times 10^{12}$	$1.183744 \times 10^{10}$
$C_{\text{fwd}}$	forward, both directions	$C_{\text{lin}} + C_{\text{norm}} + 2C_{\text{mm}}$	$2.242073591808 \times 10^{12}$	$2.81417728 \times 10^{10}$
$C_{\text{bwd}}$	backward to end-point heads and $\tau$	$\approx 2 (C_{\text{lin}} + 2C_{\text{mm}})$	$4.483945857024 \times 10^{12}$	$5.6262656 \times 10^{10}$
$C_{\text{fb}}$	forward + backward	$C_{\text{fwd}} + C_{\text{bwd}}$	$6.726019448832 \times 10^{12}$	$8.44044288 \times 10^{10}$
$C_{\text{jvp}}$	JVP cost upper bound <sup>†</sup>	$\approx 2 C_{\text{fwd}}$	$4.484147183616 \times 10^{12}$	$5.62835456 \times 10^{10}$
$C_{\text{proto-eval}}$	eval prototypes only	$C_{\text{lin}}(B_{\text{eval}}) + C_{\text{norm}}(B_{\text{eval}})$	$4.4668928 \times 10^9$	

Table 5. Batch-level FLOPs primitives and instantiated costs. Symmetric CLIP loss computes logits in both directions. <sup>†</sup> $C_{\text{jvp}}$  uses the empirical bound  $C_{\text{jvp}} \approx 2 C_{\text{fwd}}$  for this architecture and batching.

Model	Diabetic	PCAM	LC25000	Pollen	Amyloid CAA	Amyloid Diffuse	BloodMNIST	ChestMNIST
PubMedCLIP	63.25	51.46	8.16	25.27	94.12	26.88	8.45	19.01
BioMedCLIP	2.26	47.53	20.19	72.91	1.65	87.92	10.14	3.43
BMCLIP	69.95	73.96	38.00	17.28	1.80	74.72	9.44	8.77
Vanilla	2.58	55.77	20.15	10.56	52.61	63.31	17.95	57.67
Full Dataset	60.89	71.62	44.83	9.81	88.30	77.27	23.33	62.11
<i>r=10%</i>								
Random	67.29	68.43	38.91	10.18	19.85	68.07	20.61	8.44
Concept-Balance	61.18	66.89	39.71	10.87	11.07	82.57	21.81	15.62
Concept-Filter	54.91	68.60	40.00	11.06	6.85	82.21	23.41	9.93
CLIPScore	2.49	60.68	40.67	10.56	72.81	55.49	20.99	27.80
Dot	71.67	57.20	39.89	23.51	72.64	18.34	16.87	5.50
TracIn	65.40	56.75	40.03	26.34	90.73	12.84	16.69	3.69
TRAK	43.23	59.23	39.57	12.88	77.16	14.74	25.93	3.60
<b>CHIPS (ours)</b>	68.35	63.66	40.51	25.96	88.06	12.38	21.43	6.24
<i>r=20%</i>								
Random	65.86	57.13	40.55	11.13	10.30	62.52	21.92	15.43
Concept-Balance	55.50	69.32	40.13	10.37	3.49	82.83	24.00	15.01
Concept-Filter	54.92	69.78	41.04	15.21	3.25	68.44	25.46	6.93
CLIPScore	4.34	59.92	47.44	11.25	48.38	16.31	18.82	11.17
Dot	72.11	60.07	31.49	33.63	62.01	45.43	13.30	11.07
TracIn	72.77	57.24	36.61	19.17	75.28	16.98	19.70	3.00
TRAK	71.76	58.73	41.71	28.16	42.51	15.15	16.75	3.31
<b>CHIPS (ours)</b>	72.50	68.67	48.07	30.36	53.58	23.50	22.49	13.97
<i>r=30%</i>								
Random	70.95	70.79	41.39	10.94	29.82	64.34	18.42	14.17
Concept-Balance	55.50	62.83	41.01	10.43	5.07	66.69	24.61	10.15
Concept-Filter	54.92	52.14	41.15	21.06	5.73	76.31	25.96	3.97
CLIPScore	16.89	53.70	44.16	11.94	29.20	23.78	13.94	5.59
Dot	70.35	57.56	32.45	20.74	44.69	25.38	15.40	6.39
TracIn	72.13	58.48	29.81	22.19	50.72	31.45	14.24	7.28
TRAK	69.39	59.76	42.11	25.14	35.00	16.40	16.92	1.64
<b>CHIPS (ours)</b>	73.42	73.66	49.88	36.34	67.90	25.15	25.02	14.39
<i>r=50%</i>								
Random	63.57	72.99	39.65	10.56	12.41	69.59	18.82	17.01

Table 6. Full medical-domain results (Part 1/2) of the main experiment.

Model	ChestXray14	Derma	Oct	OrganA	OrganC	OrganS	Path	Retina	Tissue
PubMedCLIP	12.83	9.63	26.50	23.07	22.63	23.81	21.73	18.00	8.45
BioMedCLIP	9.78	1.20	25.00	20.28	22.55	21.92	8.48	16.00	4.66
BMCLIP	9.57	61.65	25.70	27.15	20.37	21.35	43.52	19.75	5.02
Vanilla	9.35	10.82	26.40	10.42	9.91	11.46	22.21	18.75	5.24
Full Dataset	8.64	11.72	21.50	17.51	14.89	14.20	40.91	17.50	12.40
<i>r=10%</i>									
Random	6.57	11.27	23.00	13.80	10.35	10.49	25.75	17.75	4.68
Concept-Balance	7.63	11.67	21.60	15.07	11.14	11.09	27.49	16.75	5.03
Concept-Filter	7.44	11.72	22.30	14.79	10.43	11.46	31.98	17.00	5.14
CLIPScore	6.86	11.47	27.20	8.51	8.99	11.60	25.79	16.75	5.25
Dot	6.17	12.17	20.60	9.48	10.36	11.19	25.42	33.75	4.16
TracIn	6.53	12.02	18.00	13.98	12.85	15.28	22.98	40.50	4.96
TRAK	25.84	12.17	20.90	10.74	10.43	11.22	28.68	26.75	4.46
<b>CHIPS (ours)</b>	16.63	11.87	18.20	12.03	9.64	10.71	23.90	30.25	5.29
<i>r=20%</i>									
Random	17.84	11.62	24.00	14.75	10.13	10.93	29.86	17.50	6.60
Concept-Balance	9.46	11.97	25.30	17.65	13.19	12.77	33.75	17.50	5.42
Concept-Filter	8.41	11.97	22.40	17.28	13.01	12.85	34.54	16.75	6.42
CLIPScore	4.94	11.27	27.40	10.10	11.25	11.69	22.34	20.25	4.45
Dot	7.15	11.77	22.00	12.35	12.50	12.87	25.14	23.50	5.38
TracIn	11.96	11.82	17.40	13.39	13.94	19.12	28.91	37.25	5.07
TRAK	6.94	11.02	23.50	12.42	13.49	14.43	25.10	34.50	5.41
<b>CHIPS (ours)</b>	8.96	11.87	21.40	13.50	13.80	14.87	23.20	38.50	5.92
<i>r=30%</i>									
Random	7.93	12.07	22.10	15.32	10.76	11.33	30.60	17.25	6.42
Concept-Balance	8.40	12.07	23.60	16.53	12.38	11.92	33.11	16.75	6.48
Concept-Filter	7.52	12.02	25.20	17.38	13.72	13.57	36.16	17.00	6.81
CLIPScore	4.19	11.32	26.90	9.64	11.16	10.69	28.69	22.00	4.49
Dot	10.49	11.62	21.40	13.21	12.61	12.56	30.03	23.50	7.69
TracIn	17.75	11.97	18.00	14.57	14.57	16.74	33.68	28.75	5.69
TRAK	6.49	11.42	19.20	13.80	14.61	15.91	22.98	28.25	7.75
<b>CHIPS (ours)</b>	10.65	11.37	21.30	13.13	14.28	15.33	24.43	30.25	7.69
<i>r=50%</i>									
Random	9.86	11.82	22.60	16.86	12.66	12.90	35.31	17.25	10.06

Table 7. Full medical-domain results (Part 2/2) of the main experiment. Abbreviations: Derma = DermaMNIST, Oct = OctMNIST, OrganA = OrganAMNIST, OrganC = OrganCMNIST, OrganS = OrganSMNIST, Path = PathMNIST, Retina = RetinaMNIST, Tissue = TissueMNIST.

## H.2. Generalization Experiment

The full results of the main experiment are detailed in Tab. 12 and Tab. 13 for the medical domain, and in Tab. 14 through Tab. 17 for the general domain.

## H.3. Ablation Experiment

The full results of the main experiment are detailed in Tab. 18 and Tab. 19 for the medical domain, and in Tab. 20 through Tab. 23 for the general domain.

## H.4. Analysis Experiment

- **Hyperparameter Analysis:** The analysis of evaluation set size, mixing hyperparameter  $\alpha$ , and balance hyperpa-

rameter  $\beta$  is presented in Tab. 24 through Tab. 29.

- **End-point Subspace:** The analysis of the end-point subspace  $\vartheta$  is shown in Tab. 30 and Tab. 31.
- **JL Random Projection:** The analysis of JL random projection is provided in Tab. 32 and Tab. 33.

## I. Additional Results

We provide additional experiments on MedTrinity [56] in Tab. 34 and Tab. 35.

Model	Cars	Country211	FER	Aircraft	Food101	GTSRB	Imagenet -A	Imagenet -O	Imagenet 1k	Imagenet v2
PubMedCLIP	8.51	3.09	20.30	4.32	15.43	15.37	4.97	14.55	14.95	13.00
BioMedCLIP	0.37	0.37	13.33	1.02	0.99	2.49	0.72	0.75	0.07	0.07
BMCLIP	92.13	27.18	37.57	31.38	90.40	56.22	54.93	33.85	71.97	64.80
Vanilla	74.29	22.41	42.57	28.50	87.24	43.80	46.97	39.55	70.78	62.59
Full Dataset	66.11	20.41	45.00	20.37	81.00	36.94	42.24	37.60	66.28	58.90
<i>r=10%</i>										
Random	71.43	21.76	43.73	27.06	84.99	41.94	45.60	39.20	69.18	61.31
Concept-Balance	71.28	21.81	44.90	27.48	84.82	42.76	45.73	39.35	69.12	61.05
Concept-Filter	70.92	21.61	43.86	26.91	84.59	42.36	44.91	39.30	68.75	60.85
CLIPScore	74.93	22.42	42.09	28.77	86.90	44.25	47.16	39.65	70.60	62.63
Dot	65.32	17.74	38.12	19.98	76.25	29.78	37.57	31.10	60.91	53.14
TracIn	64.82	17.30	35.94	19.71	74.90	27.40	36.41	29.95	59.22	51.16
TRAK	65.10	17.69	37.46	20.58	76.27	28.89	37.61	30.15	60.54	52.58
<b>CHIPS (ours)</b>	65.61	17.80	38.72	20.43	75.94	29.65	38.13	30.25	61.07	53.01
<i>r=20%</i>										
Random	70.20	21.60	45.29	25.71	84.47	41.35	45.23	39.30	68.67	60.53
Concept-Balance	69.12	21.29	45.89	25.77	83.75	39.30	44.53	38.40	68.26	60.30
Concept-Filter	69.42	21.20	44.61	25.89	83.36	38.61	44.03	38.40	67.87	59.94
CLIPScore	71.88	20.70	41.32	26.79	85.41	41.09	45.59	35.95	68.13	60.13
Dot	70.84	18.83	39.24	22.86	81.28	29.65	40.45	31.75	63.04	55.01
TracIn	69.54	18.55	39.29	22.23	80.37	29.30	39.48	30.55	62.51	54.46
TRAK	69.44	18.79	37.98	23.34	80.05	31.58	41.32	31.85	63.56	55.44
<b>CHIPS (ours)</b>	69.32	19.54	39.40	24.36	80.05	31.06	40.33	32.10	62.97	55.01
<i>r=30%</i>										
Random	69.36	21.36	46.22	25.23	84.10	39.74	44.61	38.40	68.21	60.20
Concept-Balance	69.03	21.50	46.20	25.92	83.55	38.97	44.56	38.60	68.33	60.48
Concept-Filter	68.88	20.82	43.81	25.08	82.21	36.93	42.68	37.75	67.13	59.44
CLIPScore	72.11	20.48	42.05	26.46	84.78	38.42	44.92	35.40	67.68	59.30
Dot	69.36	18.16	37.94	22.47	79.58	27.87	39.15	30.40	61.90	53.53
TracIn	68.96	18.20	39.84	22.89	79.51	29.26	39.65	30.15	61.87	53.63
TRAK	68.82	18.36	38.63	23.91	79.20	30.37	39.47	30.75	62.41	54.55
<b>CHIPS (ours)</b>	68.30	18.39	37.89	23.46	79.27	30.36	38.96	31.40	62.33	54.45
<i>r=50%</i>										
Random	68.47	21.03	46.15	23.28	82.96	38.74	43.67	37.90	67.61	59.90

Table 8. Full general-domain results (Part 1/4) of the main experiment.

Model	MNIST	Rendered SST2	STL10	Sun397	Sun397 Official	VOC	Caltech101	CIFAR10	CIFAR100
PubMedCLIP	25.55	54.37	59.24	18.27	16.86	34.95	22.73	38.40	10.54
BioMedCLIP	9.58	50.08	9.70	0.36	0.24	3.55	0.51	10.31	1.19
BMCLIP	86.27	63.92	97.86	69.79	69.28	80.87	83.55	96.98	81.53
Vanilla	47.83	60.57	97.28	66.83	68.20	72.18	83.80	90.24	66.69
Full Dataset	27.61	55.24	97.29	65.17	65.64	66.12	83.73	91.43	66.79
<i>r=10%</i>									
Random	45.07	55.85	97.05	66.82	67.89	69.95	85.55	91.94	67.61
Concept-Balance	37.41	54.26	97.12	67.01	68.09	69.44	85.85	92.34	68.40
Concept-Filter	41.63	56.29	96.96	66.88	67.80	69.87	85.55	92.25	67.94
CLIPScore	47.82	60.57	97.28	66.82	68.45	72.70	84.40	90.83	67.90
Dot	38.78	55.63	95.54	58.91	61.10	68.78	81.79	85.03	58.04
TracIn	39.09	52.94	95.24	57.33	59.55	68.56	82.17	82.60	54.60
TRAK	44.99	56.84	95.80	58.33	60.34	66.35	83.22	82.17	54.39
<b>CHIPS (ours)</b>	38.82	57.84	94.91	58.00	57.88	68.66	82.48	80.76	55.33
<i>r=20%</i>									
Random	34.08	54.48	97.17	66.71	67.57	67.92	85.39	92.22	67.98
Concept-Balance	38.87	55.68	97.14	66.54	67.39	67.91	85.09	91.96	67.62
Concept-Filter	36.40	57.11	96.88	66.43	66.99	69.49	85.19	91.68	67.26
CLIPScore	47.78	58.54	97.04	62.08	64.06	71.39	83.63	88.03	61.89
Dot	38.50	57.77	95.36	56.67	59.19	66.22	81.61	84.61	57.69
TracIn	37.95	55.19	94.67	56.22	58.38	67.15	81.71	84.93	56.99
TRAK	43.87	51.62	95.14	55.84	58.63	68.10	82.04	85.28	58.14
<b>CHIPS (ours)</b>	42.91	50.63	95.42	55.94	58.51	65.89	81.38	85.72	59.00
<i>r=30%</i>									
Random	27.07	54.26	97.15	66.51	67.18	67.28	85.08	92.34	68.13
Concept-Balance	31.72	54.31	97.00	66.68	67.37	68.08	85.09	92.18	68.32
Concept-Filter	34.15	57.33	96.80	65.84	66.55	68.56	84.34	91.07	65.50
CLIPScore	46.31	57.06	97.05	62.11	63.81	69.97	83.32	88.35	62.38
Dot	37.90	54.64	95.31	55.82	57.89	66.75	80.82	83.64	55.78
TracIn	37.04	53.21	94.96	55.72	57.92	67.11	80.84	83.05	54.84
TRAK	32.68	50.08	95.30	55.68	57.78	64.52	80.81	84.56	57.45
<b>CHIPS (ours)</b>	34.25	49.92	95.36	55.69	57.91	64.36	80.79	84.61	57.64
<i>r=50%</i>									
Random	30.17	54.09	97.21	66.02	66.73	66.76	84.60	92.11	67.94

Table 9. Full general-domain results (Part 2/4) of the main experiment.

Model	CLEVR Closest	CLEVR Count	DMLAB	DTD	Eurosat	Flowers	KITTI
PubMedCLIP	22.28	16.23	18.85	10.59	19.70	14.54	31.36
BioMedCLIP	24.51	16.85	16.86	1.17	11.26	0.59	29.54
BMCLIP	15.79	33.98	13.80	55.64	63.02	76.11	26.30
Vanilla	22.47	29.11	16.11	56.22	55.96	73.57	24.47
Full Dataset	20.45	21.03	12.08	50.48	50.06	70.69	32.49
<i>r=10%</i>							
Random	22.57	29.39	12.28	53.56	53.31	72.68	31.08
Concept-Balance	22.59	31.12	12.02	52.93	52.39	72.94	28.83
Concept-Filter	22.41	31.32	11.99	52.66	48.26	72.68	29.54
CLIPScore	22.45	31.71	15.08	56.60	56.54	74.21	22.93
Dot	21.38	25.25	15.86	47.82	42.61	66.14	17.58
TracIn	21.39	22.96	14.83	45.80	40.17	66.08	17.02
TRAK	22.55	21.23	14.04	48.14	37.98	68.12	20.82
<b>CHIPS (ours)</b>	22.59	21.31	14.92	48.86	40.27	66.29	19.83
<i>r=20%</i>							
Random	22.16	26.30	11.98	52.66	51.19	73.05	30.66
Concept-Balance	21.53	29.22	11.80	52.07	52.26	72.48	29.68
Concept-Filter	21.51	30.64	11.92	51.91	50.33	71.74	31.50
CLIPScore	22.47	28.19	14.92	55.00	48.13	70.60	20.39
Dot	20.93	20.89	16.73	46.44	41.33	65.67	20.39
TracIn	18.71	21.03	15.45	43.88	40.69	64.55	16.60
TRAK	21.21	24.05	15.61	45.11	41.83	66.45	18.71
<b>CHIPS (ours)</b>	21.52	25.25	16.21	44.47	42.89	66.53	16.46
<i>r=30%</i>							
Random	21.86	26.93	11.85	52.34	52.33	72.56	32.07
Concept-Balance	21.23	27.33	11.83	51.44	52.69	72.56	30.38
Concept-Filter	21.63	27.87	11.84	51.65	48.91	71.59	31.50
CLIPScore	22.44	27.65	14.88	55.11	47.78	70.92	18.00
Dot	21.01	20.81	15.41	42.82	39.65	64.90	16.60
TracIn	18.77	20.52	15.44	43.14	37.85	65.05	17.02
TRAK	21.40	20.57	15.64	44.26	41.35	64.68	15.61
<b>CHIPS (ours)</b>	21.60	20.78	15.76	44.20	42.19	65.30	14.77
<i>r=50%</i>							
Random	21.29	24.69	11.74	51.38	50.54	71.85	32.77

Table 10. Full general-domain results (Part 3/4) of the main experiment.

Model	Pets	RESISC45	Smallnorb Azimuth	Smallnorb Elevation	SVHN
PubMedCLIP	23.36	14.22	5.51	10.97	7.43
BioMedCLIP	2.89	2.21	5.64	10.95	9.83
BMCLIP	91.39	63.38	6.29	10.54	50.43
Vanilla	90.54	66.08	5.42	10.92	24.34
Full Dataset	88.77	63.05	6.77	12.12	19.39
<i>r=10%</i>					
Random	90.52	64.08	5.93	10.88	18.41
Concept-Balance	90.11	63.76	5.82	10.47	19.17
Concept-Filter	89.83	62.35	5.82	10.53	19.56
CLIPScore	90.02	66.38	5.67	11.51	25.80
Dot	88.09	60.21	5.84	10.44	26.41
TracIn	88.23	60.14	5.47	11.37	24.96
TRAK	87.57	60.54	5.26	11.60	26.31
<b>CHIPS (ours)</b>	86.97	58.44	5.55	11.82	25.23
<i>r=20%</i>					
Random	90.16	63.87	6.11	10.97	18.19
Concept-Balance	89.45	63.49	6.07	11.05	18.78
Concept-Filter	89.32	61.79	5.90	11.12	20.29
CLIPScore	89.02	64.83	5.34	10.80	27.57
Dot	86.48	60.22	6.51	10.48	25.77
TracIn	88.25	59.75	5.37	10.96	25.78
TRAK	86.59	60.29	5.67	11.80	24.32
<b>CHIPS (ours)</b>	87.24	59.68	5.49	11.02	24.63
<i>r=30%</i>					
Random	89.92	63.79	6.27	10.74	17.19
Concept-Balance	89.29	64.56	6.41	10.78	18.74
Concept-Filter	89.23	62.60	5.97	11.74	20.28
CLIPScore	88.39	64.11	5.13	10.89	26.40
Dot	86.59	60.65	5.69	11.64	23.29
TracIn	87.76	59.51	5.54	10.67	23.28
TRAK	86.84	59.44	5.60	11.30	23.07
<b>CHIPS (ours)</b>	87.08	60.00	5.84	11.18	22.45
<i>r=50%</i>					
Random	89.64	63.71	6.19	11.04	17.09

Table 11. Full general-domain results (Part 4/4) of the main experiment.

Model	Diabetic	PCAM	LC25000	Pollen	Amyloid CAA	Amyloid Diffuse	BloodMNIST	ChestMNIST
<i>B32-400M</i>								
Random	53.80	65.05	40.88	67.57	93.21	23.61	14.56	1.24
TracIn	57.38	55.25	37.12	50.47	96.33	12.32	21.66	2.16
<b>CHIPS (ours)</b>	59.94	55.22	36.27	69.83	98.35	13.97	16.22	1.56
<i>B32-CC</i>								
Random	73.20	62.22	21.31	32.24	1.54	87.94	35.52	3.53
TracIn	66.56	56.44	19.17	23.26	5.01	85.16	30.20	11.05
<b>CHIPS (ours)</b>	51.66	56.75	19.44	39.85	6.46	87.88	28.73	34.37
<i>B16-400M</i>								
Random	67.29	68.43	38.91	10.18	19.85	68.07	20.61	8.44
TracIn	65.40	56.75	40.03	26.34	90.73	12.84	16.69	3.69
<b>CHIPS (ours)</b>	68.35	63.66	40.51	25.96	88.06	12.38	21.43	6.24
<i>B16-CC</i>								
Random	72.85	59.01	20.61	16.66	49.21	87.68	16.90	2.33
TracIn	74.49	52.07	20.33	19.04	91.57	37.16	12.36	2.00
<b>CHIPS (ours)</b>	76.91	54.99	32.75	22.88	34.65	82.59	14.88	2.90
<i>L14-400M</i>								
Random	73.65	55.76	43.68	19.61	11.95	87.16	9.97	5.72
TracIn	65.62	60.57	40.61	16.03	18.51	51.40	19.47	5.10
<b>CHIPS (ours)</b>	65.34	61.27	39.65	19.48	44.86	73.60	11.14	5.84
<i>L14-CC</i>								
Random	47.71	54.50	24.16	68.13	11.29	86.15	18.06	41.76
TracIn	51.44	56.73	26.40	60.72	42.54	83.83	18.80	49.22
<b>CHIPS (ours)</b>	54.22	56.09	21.73	63.54	33.75	84.75	20.50	46.61
<i>H14-CC</i>								
Random	72.41	64.77	50.27	12.19	92.56	86.96	24.44	2.43
TracIn	73.09	65.87	50.75	12.70	76.15	83.24	14.24	2.92
<b>CHIPS (ours)</b>	78.64	65.30	55.12	11.50	82.87	86.85	20.94	8.00

Table 12. Full medical-domain results (Part 1/2) of the generalization experiment.

Model	ChestXray14	Derma	Oct	OrganA	OrganC	OrganS	Path	Retina	Tissue
<i>B32-400M</i>									
Random	6.05	13.97	25.00	10.77	6.86	5.30	34.50	9.75	5.31
TracIn	3.80	17.11	24.80	9.93	10.32	9.19	16.56	36.00	12.49
<b>CHIPS (ours)</b>	2.64	12.52	24.20	13.31	11.33	10.59	27.87	19.25	11.63
<i>B32-CC</i>									
Random	4.42	9.63	25.00	16.22	8.98	6.24	31.91	14.25	9.18
TracIn	6.71	16.06	24.30	18.37	11.37	11.03	27.80	19.00	10.78
<b>CHIPS (ours)</b>	9.14	13.82	24.70	23.67	14.28	13.67	29.82	13.00	10.36
<i>B16-400M</i>									
Random	6.57	11.27	23.00	13.80	10.35	10.49	25.75	17.75	4.68
TracIn	6.53	12.02	18.00	13.98	12.85	15.28	22.98	40.50	4.96
<b>CHIPS (ours)</b>	16.63	11.87	18.20	12.03	9.64	10.71	23.90	30.25	5.29
<i>B16-CC</i>									
Random	9.92	11.82	25.50	17.61	11.04	12.47	31.50	6.00	5.38
TracIn	9.12	12.82	23.30	14.47	14.05	15.37	41.14	8.50	5.94
<b>CHIPS (ours)</b>	10.10	12.37	24.20	13.61	13.56	14.42	43.15	9.75	6.22
<i>L14-400M</i>									
Random	9.81	19.10	23.20	26.17	16.99	17.37	36.39	38.50	23.02
TracIn	10.51	21.05	23.30	23.10	16.13	17.55	36.92	31.00	11.04
<b>CHIPS (ours)</b>	8.74	25.74	22.20	23.01	15.06	17.07	35.04	38.50	17.37
<i>L14-CC</i>									
Random	13.06	21.40	26.20	25.68	19.81	19.23	30.74	20.25	7.31
TracIn	15.82	27.83	23.60	16.71	15.68	11.29	21.88	20.25	6.11
<b>CHIPS (ours)</b>	16.39	28.99	23.30	19.39	16.38	15.26	25.42	16.75	7.74
<i>H14-CC</i>									
Random	8.97	62.19	24.80	25.52	16.69	14.35	38.29	8.00	4.83
TracIn	13.05	64.69	23.80	31.44	20.53	18.83	37.51	22.25	6.53
<b>CHIPS (ours)</b>	8.89	54.16	23.20	27.00	18.78	15.67	34.21	19.25	7.24

Table 13. Full medical-domain results (Part 2/2) of the generalization experiment.

Model	Cars	Country211	FER	Aircraft	Food101	GTSRB	Imagenet -A	Imagenet -O	Imagenet 1k	Imagenet v2
<i>B32-400M</i>										
Random	66.66	16.73	30.54	25.44	78.84	38.45	27.85	45.80	63.49	55.78
TracIn	66.00	15.50	33.74	22.41	77.07	27.69	27.07	40.75	61.35	52.69
<b>CHIPS (ours)</b>	65.97	15.85	31.51	24.42	77.74	30.26	28.40	42.10	62.46	53.85
<i>B32-CC</i>										
Random	74.99	17.20	43.52	23.34	80.65	39.71	28.37	46.35	65.90	57.95
TracIn	73.96	15.58	35.82	23.46	78.49	37.19	29.13	40.85	63.71	55.60
<b>CHIPS (ours)</b>	73.37	16.05	45.75	24.15	79.41	35.33	29.73	41.55	64.16	56.40
<i>B16-400M</i>										
Random	71.43	21.76	43.73	27.06	84.99	41.94	45.60	39.20	69.18	61.31
TracIn	70.63	19.09	37.11	23.91	81.94	31.37	40.48	31.20	63.62	55.34
<b>CHIPS (ours)</b>	68.40	21.47	40.69	25.32	82.60	31.02	42.36	32.50	66.88	56.22
<i>B16-CC</i>										
Random	81.12	22.35	48.75	30.42	86.97	51.00	48.59	40.85	71.06	64.12
TracIn	75.25	17.76	34.20	22.59	81.33	36.29	41.97	31.20	62.65	55.68
<b>CHIPS (ours)</b>	75.96	18.10	35.33	23.49	82.34	40.96	43.88	32.20	64.15	57.34
<i>L14-400M</i>										
Random	82.93	30.34	41.36	38.97	89.35	48.79	65.73	29.35	75.23	68.72
TracIn	78.54	26.27	36.57	35.25	87.81	39.90	61.49	24.30	69.84	63.35
<b>CHIPS (ours)</b>	80.26	26.73	39.45	34.71	88.02	41.71	62.24	25.20	70.88	64.61
<i>L14-CC</i>										
Random	88.02	33.86	54.99	42.18	93.31	56.33	71.47	29.05	78.28	71.32
TracIn	83.62	29.36	46.68	41.19	90.38	48.76	66.41	24.65	73.51	66.43
<b>CHIPS (ours)</b>	84.65	29.78	47.94	40.98	91.25	46.98	68.07	25.15	74.15	67.55
<i>H14-CC</i>										
Random	89.64	37.46	52.49	51.43	93.87	58.34	74.92	29.45	79.75	73.69
TracIn	88.73	35.35	53.19	45.15	92.81	57.78	73.16	24.05	76.19	69.91
<b>CHIPS (ours)</b>	88.30	35.64	55.46	47.58	93.09	57.86	74.25	24.85	76.63	70.39

Table 14. Full general-domain results (Part 1/4) of the generalization experiment.

Model	MNIST	Rendered SST2	STL10	Sun397	Sun397 Official	VOC	Caltech101	CIFAR10	CIFAR100
<i>B32-400M</i>									
Random	39.99	54.81	96.11	63.75	64.66	66.37	84.21	91.19	67.92
TracIn	35.04	53.76	94.42	59.56	60.19	68.32	82.86	88.24	63.02
<b>CHIPS (ours)</b>	38.52	55.13	95.08	59.43	60.70	66.67	82.70	88.68	63.70
<i>B32-CC</i>									
Random	43.11	53.87	96.42	66.50	66.95	76.30	85.80	95.17	77.92
TracIn	38.90	52.83	95.40	63.29	64.03	75.01	86.06	94.27	76.24
<b>CHIPS (ours)</b>	36.16	51.62	95.71	63.95	64.63	75.73	84.62	94.01	75.47
<i>B16-400M</i>									
Random	45.07	55.85	97.05	66.82	67.89	69.95	85.55	91.94	67.61
TracIn	39.09	52.94	95.24	57.33	59.55	68.56	82.17	82.60	54.60
<b>CHIPS (ours)</b>	38.82	57.84	94.91	58.00	57.88	68.66	82.48	80.76	55.33
<i>B16-CC</i>									
Random	59.17	54.75	98.35	68.43	69.29	78.17	84.54	96.09	79.97
TracIn	54.70	53.27	97.12	58.73	60.19	69.29	82.28	92.97	72.27
<b>CHIPS (ours)</b>	55.66	54.42	97.61	61.01	62.31	70.19	82.68	93.50	73.19
<i>L14-400M</i>									
Random	52.89	64.52	99.20	71.34	72.54	74.47	85.98	95.97	76.67
TracIn	58.40	58.26	97.34	62.08	63.28	62.04	82.28	89.52	70.96
<b>CHIPS (ours)</b>	59.23	62.93	97.74	61.34	62.34	62.95	82.83	91.16	70.80
<i>L14-CC</i>									
Random	60.93	68.26	99.25	72.03	73.77	80.58	88.15	97.60	84.84
TracIn	57.61	56.73	98.61	66.52	67.98	74.63	84.45	95.20	79.35
<b>CHIPS (ours)</b>	64.90	64.80	98.84	67.41	68.64	75.45	84.42	95.46	78.86
<i>H14-CC</i>									
Random	70.45	70.68	99.49	73.01	75.34	73.45	87.54	98.10	86.61
TracIn	33.99	66.89	99.19	68.30	69.37	67.22	83.43	97.15	84.05
<b>CHIPS (ours)</b>	20.47	63.87	99.20	68.98	70.47	69.35	85.18	97.09	84.10

Table 15. Full general-domain results (Part 2/4) of the generalization experiment.

Model	CLEVR Closest	CLEVR Count	DMLAB	DTD	Eurosat	Flowers	KITTI
<i>B32-400M</i>							
Random	21.01	23.33	19.06	50.32	50.06	70.06	32.63
TracIn	21.85	22.33	16.89	47.55	47.96	66.60	24.61
<b>CHIPS (ours)</b>	22.40	23.06	15.15	48.30	45.43	69.15	32.07
<i>B32-CC</i>							
Random	23.78	21.09	12.20	55.64	49.52	69.07	15.33
TracIn	22.59	19.37	12.34	53.03	45.76	63.77	15.61
<b>CHIPS (ours)</b>	22.55	20.12	13.17	54.52	43.00	66.11	19.69
<i>B16-400M</i>							
Random	22.57	29.39	12.28	53.56	53.31	72.68	31.08
TracIn	21.39	22.96	14.83	45.80	40.17	66.08	17.02
<b>CHIPS (ours)</b>	22.59	21.31	14.92	48.86	40.27	66.29	19.83
<i>B16-CC</i>							
Random	22.55	28.51	21.39	61.65	52.61	74.94	27.00
TracIn	22.69	25.08	19.25	51.60	53.44	62.06	22.22
<b>CHIPS (ours)</b>	22.72	26.79	19.38	52.87	55.43	65.07	22.08
<i>L14-400M</i>							
Random	21.07	34.80	20.12	59.84	62.15	77.90	28.41
TracIn	22.93	27.41	19.26	51.97	50.56	73.78	30.38
<b>CHIPS (ours)</b>	23.67	27.62	17.88	53.72	50.19	75.05	29.54
<i>L14-CC</i>							
Random	22.54	28.61	16.64	66.38	66.76	81.53	24.33
TracIn	22.54	27.45	20.95	59.89	56.39	78.09	25.04
<b>CHIPS (ours)</b>	22.54	28.74	18.50	60.37	53.33	78.60	32.77
<i>H14-CC</i>							
Random	10.25	20.78	14.86	68.99	69.37	83.72	27.14
TracIn	21.85	23.17	13.62	63.24	62.37	81.18	22.93
<b>CHIPS (ours)</b>	20.85	21.61	13.02	66.17	61.69	81.43	25.32

Table 16. Full general-domain results (Part 3/4) of the generalization experiment.

Model	Pets	RESISC45	Smallnorb Azimuth	Smallnorb Elevation	SVHN
<i>B32-400M</i>					
Random	85.75	57.11	5.35	12.03	23.40
TracIn	84.79	55.87	5.74	11.45	27.67
<b>CHIPS (ours)</b>	86.67	56.70	5.24	12.04	25.37
<i>B32-CC</i>					
Random	88.74	59.37	5.70	12.20	18.77
TracIn	87.84	56.25	5.60	11.65	22.40
<b>CHIPS (ours)</b>	88.47	58.83	6.09	12.47	21.03
<i>B16-400M</i>					
Random	90.52	64.08	5.93	10.88	18.41
TracIn	88.23	60.14	5.47	11.37	24.96
<b>CHIPS (ours)</b>	86.97	58.44	5.55	11.82	25.23
<i>B16-CC</i>					
Random	91.09	66.79	4.95	10.77	37.11
TracIn	87.57	59.35	5.33	11.01	36.07
<b>CHIPS (ours)</b>	87.82	60.21	5.28	10.77	36.69
<i>L14-400M</i>					
Random	92.89	68.68	5.51	11.04	22.41
TracIn	90.30	63.06	5.93	11.94	27.65
<b>CHIPS (ours)</b>	91.41	63.32	5.85	12.17	27.55
<i>L14-CC</i>					
Random	94.06	75.13	4.85	11.13	46.73
TracIn	90.81	66.89	5.40	11.11	49.62
<b>CHIPS (ours)</b>	92.37	66.44	5.21	11.56	50.27
<i>H14-CC</i>					
Random	95.53	72.56	6.30	12.30	44.79
TracIn	94.19	68.65	5.82	12.40	50.89
<b>CHIPS (ours)</b>	94.49	68.44	6.44	12.21	50.99

Table 17. Full general-domain results (Part 4/4) of the generalization experiment.

Model	Diabetic	PCAM	LC25000	Pollen	Amyloid CAA	Amyloid Diffuse	BloodMNIST	ChestMNIST
<i>r=10%</i>								
Alignment-only	59.51	57.64	39.41	12.76	88.69	13.17	23.62	3.71
Alignment-Margin	59.56	57.65	40.21	11.69	87.51	13.94	23.56	3.26
<b>CHIPS (ours)</b>	68.35	63.66	40.51	25.96	88.06	12.38	21.43	6.24
<i>r=20%</i>								
Alignment-only	72.41	68.04	46.98	30.54	55.27	21.32	20.56	12.24
Alignment-Margin	72.02	68.32	46.87	30.10	58.24	21.65	21.34	12.34
<b>CHIPS (ours)</b>	72.50	68.67	48.07	30.36	53.58	23.50	22.49	13.97
<i>r=30%</i>								
Alignment-only	71.30	72.76	43.79	32.14	60.26	22.71	21.88	11.77
Alignment-Margin	71.24	70.43	48.16	32.42	61.79	25.12	23.44	13.19
<b>CHIPS (ours)</b>	73.42	73.66	49.88	36.34	67.90	25.15	25.02	14.39

Table 18. Full medical-domain results (Part 1/2) of the ablation experiment.

Model	ChestXray14	Derma	Oct	OrganA	OrganC	OrganS	Path	Retina	Tissue
<i>r=10%</i>									
Alignment-only	21.49	12.07	20.20	11.65	10.08	10.81	27.28	27.00	4.86
Alignment-Margin	21.02	12.17	19.60	12.10	10.00	10.28	26.70	29.25	4.99
<b>CHIPS (ours)</b>	16.63	11.87	18.20	12.03	9.64	10.71	23.90	30.25	5.29
<i>r=20%</i>									
Alignment-only	9.57	11.22	20.80	14.10	13.86	15.24	24.57	32.00	5.99
Alignment-Margin	9.07	11.12	20.80	14.53	14.17	15.04	24.55	35.75	5.39
<b>CHIPS (ours)</b>	8.96	11.87	21.40	13.50	13.80	14.87	23.20	38.50	5.92
<i>r=30%</i>									
Alignment-only	8.28	11.22	21.80	13.62	12.99	14.87	21.56	30.75	7.46
Alignment-Margin	10.49	11.32	20.50	14.35	13.38	12.69	24.08	30.50	6.40
<b>CHIPS (ours)</b>	10.65	11.37	21.30	13.13	14.28	15.33	24.43	30.25	7.69

Table 19. Full medical-domain results (Part 2/2) of the ablation experiment.

Model	Cars	Country211	FER	Aircraft	Food101	GSTRB	Imagenet -A	Imagenet -O	Imagenet 1k	Imagenet v2
<i>r=10%</i>										
Alignment-only	69.99	19.50	40.85	25.59	82.55	31.56	42.47	32.95	64.84	56.63
Alignment-Margin	70.12	21.67	40.81	25.92	82.60	31.62	42.17	32.45	65.01	56.78
<b>CHIPS (ours)</b>	68.40	21.47	40.69	25.32	82.60	31.02	42.36	32.50	66.88	56.22
<i>r=20%</i>										
Alignment-only	68.97	18.80	39.19	24.60	80.06	31.50	40.11	31.60	62.95	55.05
Alignment-Margin	68.95	19.59	39.23	24.51	80.03	31.92	40.15	31.60	62.89	54.99
<b>CHIPS (ours)</b>	69.32	19.54	39.40	24.36	80.05	31.06	40.33	32.10	62.97	55.01
<i>r=30%</i>										
Alignment-only	68.86	18.41	38.35	24.78	79.45	30.78	39.45	31.60	62.63	54.52
Alignment-Margin	68.74	18.48	42.28	24.18	79.93	30.43	39.83	31.40	62.56	54.74
<b>CHIPS (ours)</b>	68.30	18.39	37.89	23.46	79.27	30.36	38.96	31.40	62.33	54.45

Table 20. Full general-domain results (Part 1/4) of the ablation experiment.

Model	MNIST	Rendered SST2	STL10	Sun397	Sun397 Official	VOC	Caltech101	CIFAR10	CIFAR100
<i>r=10%</i>									
Alignment-only	45.04	56.78	95.42	58.44	60.47	66.18	83.27	82.55	55.19
Alignment-Margin	44.47	57.44	95.34	58.34	60.40	66.66	82.93	82.57	55.34
<b>CHIPS (ours)</b>	38.82	57.84	94.91	58.00	57.88	68.66	82.48	80.76	55.33
<i>r=20%</i>									
Alignment-only	43.42	50.74	95.19	56.52	58.73	66.31	81.38	84.85	57.73
Alignment-Margin	42.65	50.36	94.99	56.47	58.76	65.93	81.10	85.76	59.11
<b>CHIPS (ours)</b>	42.91	50.63	95.42	55.94	58.51	65.89	81.38	85.72	59.00
<i>r=30%</i>									
Alignment-only	38.92	50.14	95.21	56.16	58.28	65.77	80.12	85.44	57.97
Alignment-Margin	35.97	50.03	95.17	55.95	58.43	62.85	80.30	84.61	56.85
<b>CHIPS (ours)</b>	34.25	49.92	95.36	55.69	57.91	64.36	80.79	84.61	57.64

Table 21. Full general-domain results (Part 2/4) of the ablation experiment.

Model	CLEVR Closest	CLEVR Count	DMLAB	DTD	Eurosat	Flowers	KITTI
<i>r=10%</i>							
Alignment-only	22.62	21.30	13.90	48.67	38.98	68.11	23.49
Alignment-Margin	22.58	21.41	14.14	49.36	39.11	68.01	23.21
<b>CHIPS (ours)</b>	22.59	21.31	14.92	48.86	40.27	66.29	19.83
<i>r=20%</i>							
Alignment-only	21.27	24.39	15.90	44.79	41.89	66.22	17.86
Alignment-Margin	21.00	25.33	15.90	44.26	42.15	66.30	17.44
<b>CHIPS (ours)</b>	21.52	25.25	16.21	44.47	42.89	66.53	16.46
<i>r=30%</i>							
Alignment-only	21.24	21.56	15.40	45.21	42.76	65.03	15.61
Alignment-Margin	22.24	20.59	16.86	44.15	42.06	65.67	17.72
<b>CHIPS (ours)</b>	21.60	20.78	15.76	44.20	42.19	65.30	14.77

Table 22. Full general-domain results (Part 3/4) of the ablation experiment.

Model	Pets	RESISC45	Smallnorb Azimuth	Smallnorb Elevation	SVHN
<i>r=10%</i>					
Alignment-only	87.46	60.33	5.51	11.34	26.19
Alignment-Margin	87.35	60.21	5.47	11.32	26.04
<b>CHIPS (ours)</b>	86.97	58.44	5.55	11.82	25.23
<i>r=20%</i>					
Alignment-only	87.35	59.48	5.62	11.06	24.34
Alignment-Margin	87.35	59.49	5.32	10.74	23.96
<b>CHIPS (ours)</b>	87.24	59.68	5.49	11.02	24.63
<i>r=30%</i>					
Alignment-only	86.70	59.60	5.53	10.79	23.94
Alignment-Margin	87.00	59.68	5.82	10.99	23.79
<b>CHIPS (ours)</b>	87.08	60.00	5.84	11.18	22.45

Table 23. Full general-domain results (Part 4/4) of the ablation experiment.

Model	Diabetic	PCAM	LC25000	Pollen	Amyloid CAA	Amyloid Diffuse	BloodMNIST	ChestMNIST
<i>Evaluation Set Size</i>								
50	67.33	57.66	39.68	18.10	87.22	12.69	21.51	2.79
100	57.57	58.45	39.39	14.90	82.92	13.02	24.76	2.50
150	54.62	56.38	40.61	11.38	85.64	13.07	24.06	4.61
200	68.35	63.66	40.51	25.96	88.06	12.38	21.43	6.24
250	68.07	66.49	40.55	22.20	87.99	12.63	23.91	2.14
$\alpha$								
0.2	52.04	57.57	40.53	13.70	79.23	13.61	24.55	4.28
0.4	51.45	57.18	41.20	13.51	74.95	14.03	24.90	3.28
0.6	56.65	55.74	40.21	14.39	89.81	13.85	25.17	2.90
0.8	68.35	63.66	40.51	25.96	88.06	12.38	21.43	6.24
1.0	51.01	55.88	40.67	14.77	83.71	13.51	23.79	3.29
$\beta$								
0	71.38	59.27	44.43	27.03	43.02	25.05	18.36	3.13
0.25	54.72	56.48	39.89	11.75	90.43	12.74	22.42	3.08
0.50	68.35	63.66	40.51	25.96	88.06	12.38	21.43	6.24
0.75	52.53	57.27	38.93	13.83	86.47	13.79	23.21	4.25
1.0	71.53	59.11	41.89	26.40	54.35	23.21	15.76	2.71

Table 24. Full medical-domain results (Part 1/2) of the analysis on evaluation set size,  $\alpha$ , and  $\beta$ .

Model	ChestXray14	Derma	Oct	OrganA	OrganC	OrganS	Path	Retina	Tissue
<i>Evaluation Set Size</i>									
50	16.07	12.07	21.50	8.66	8.70	10.04	26.56	35.25	5.20
100	21.20	12.17	20.70	9.23	8.87	9.49	26.24	32.75	5.87
150	28.48	12.32	21.00	11.42	10.32	10.59	30.21	35.00	4.92
200	16.63	11.87	18.20	12.03	9.64	10.71	23.90	30.25	5.29
250	16.49	12.07	19.50	12.48	10.13	9.88	24.38	30.25	5.02
$\alpha$									
0.2	30.17	12.12	20.30	10.93	9.54	10.30	28.23	30.00	4.92
0.4	29.49	12.17	20.70	10.98	10.08	10.82	28.08	29.25	4.82
0.6	28.46	12.32	20.70	11.76	10.66	11.74	29.33	33.00	4.95
0.8	16.63	11.87	18.20	12.03	9.64	10.71	23.90	30.25	5.29
1.0	28.75	12.07	20.30	11.49	10.30	11.39	29.04	30.50	5.04
$\beta$									
0	7.56	11.32	19.90	10.15	11.19	12.91	24.43	37.00	5.80
0.25	19.36	12.07	20.60	11.63	10.02	10.11	26.38	35.50	5.18
0.50	16.63	11.87	18.20	12.03	9.64	10.71	23.90	30.25	5.29
0.75	22.38	11.82	19.90	11.30	10.70	11.05	29.28	32.75	5.45
1.0	6.39	10.97	19.50	10.09	11.51	12.71	24.32	38.75	5.68

Table 25. Full medical-domain results (Part 2/2) of the analysis on evaluation set size,  $\alpha$ , and  $\beta$ .

Model	Cars	Country211	FER	Aircraft	Food101	GSTRB	Imagenet -A	Imagenet -O	Imagenet 1k	Imagenet v2
<i>Evaluation Set Size</i>										
50	70.15	19.38	40.58	25.65	82.56	31.46	42.68	33.05	65.04	57.01
100	69.79	19.40	41.70	25.26	82.52	33.02	42.25	32.10	65.15	57.00
150	69.48	19.48	41.07	24.75	82.70	32.54	42.09	33.40	64.97	56.96
200	68.40	21.47	40.69	25.32	82.60	31.02	42.36	32.50	66.88	56.22
250	67.38	19.41	40.35	25.08	82.91	30.02	42.45	32.25	64.91	56.80
$\alpha$										
0.2	69.59	19.26	41.71	24.99	82.4	32.38	42.72	32.35	64.97	56.81
0.4	69.82	19.34	40.97	25.26	82.65	32.07	42.71	32.40	65.12	57.15
0.6	68.40	21.47	40.69	25.32	82.60	31.02	42.36	32.50	66.88	56.22
0.8	69.88	19.40	40.92	25.77	82.56	31.95	42.85	31.70	65.08	57.13
1.0	70.07	19.50	41.31	25.56	82.63	31.50	43.00	32.15	65.12	57.08
$\beta$										
0	71.00	19.63	42.77	25.77	82.05	32.64	42.29	31.70	64.59	56.71
0.25	69.98	19.42	40.14	25.26	82.51	31.57	41.99	32.30	64.99	56.68
0.50	68.40	21.47	40.69	25.32	82.60	31.02	42.36	32.50	66.88	56.22
0.75	70.54	19.26	41.39	25.26	82.66	33.66	42.52	32.10	65.11	57.02
1.0	70.39	19.41	41.84	26.76	81.91	32.07	41.99	32.25	64.63	56.26

Table 26. Full general-domain results (Part 1/4) of the analysis on evaluation set size,  $\alpha$ , and  $\beta$ .

Model	MNIST	Rendered SST2	STL10	Sun397	Sun397 Official	VOC	Caltech101	CIFAR10	CIFAR100
<i>Evaluation Set Size</i>									
50	47.03	57.77	95.29	58.61	60.61	66.67	82.74	82.78	54.91
100	46.74	56.84	95.40	58.71	60.62	65.63	83.47	82.48	54.73
150	43.58	57.00	95.31	59.10	60.79	64.98	83.57	82.77	55.25
200	38.82	57.84	94.91	58.00	57.88	68.66	82.48	80.76	55.33
250	42.26	58.26	95.09	57.58	60.68	63.62	83.25	80.11	55.04
$\alpha$									
0.2	45.55	57.44	95.31	58.91	60.49	66.91	83.06	82.61	55.31
0.4	45.44	57.83	95.40	58.78	60.65	67.05	83.11	83.08	55.68
0.6	38.82	57.84	94.91	58.00	57.88	68.66	82.48	80.76	55.33
0.8	45.82	57.33	95.39	58.92	60.55	66.19	83.27	82.96	55.15
1.0	47.11	57.66	95.51	58.73	60.53	66.57	83.27	82.95	55.21
$\beta$									
0	42.85	52.33	95.51	57.74	60.47	66.73	82.65	85.81	58.97
0.25	44.89	58.26	94.31	58.89	60.89	66.29	82.97	82.37	54.13
0.50	38.82	57.84	94.91	58.00	57.88	68.66	82.48	80.76	55.33
0.75	42.92	58.37	95.34	58.86	60.79	66.25	83.58	84.02	56.88
1.0	40.30	51.89	95.14	57.72	60.44	66.75	82.51	85.63	59.00

Table 27. Full general-domain results (Part 2/4) of the analysis on evaluation set size,  $\alpha$ , and  $\beta$ .

Model	CLEVR Closest	CLEVR Count	DMLAB	DTD	Eurosat	Flowers	KITTI
<i>Evaluation Set Size</i>							
50	22.65	21.22	14.08	48.24	39.11	68.11	23.21
100	22.65	21.45	14.08	48.83	38.69	68.04	22.22
150	22.60	22.14	14.63	48.35	39.52	67.47	23.07
200	22.59	21.31	14.92	48.86	40.27	66.29	19.83
250	22.44	21.19	13.76	48.35	37.52	67.05	25.32
$\alpha$							
0.2	22.59	21.78	14.44	47.93	38.48	68.21	22.22
0.4	22.59	21.87	14.42	48.51	38.28	68.14	22.78
0.6	22.59	21.31	14.92	48.86	40.27	66.29	19.83
0.8	22.61	21.41	14.03	48.40	38.52	67.99	21.94
1.0	22.63	21.91	14.18	48.62	38.28	67.99	21.10
$\beta$							
0	22.10	26.25	15.35	46.91	42.26	68.35	20.53
0.25	22.66	21.09	13.89	48.14	39.11	68.48	23.07
0.50	22.59	21.31	14.92	48.86	40.27	66.29	19.83
0.75	22.55	21.87	13.98	47.93	37.81	67.75	23.21
1.0	22.06	26.15	15.76	47.23	42.78	68.24	20.53

Table 28. Full general-domain results (Part 3/4) of the analysis on evaluation set size,  $\alpha$ , and  $\beta$ .

Model	Pets	RESISC45	Smallnorb Azimuth	Smallnorb Elevation	SVHN
<i>Evaluation Set Size</i>					
50	87.63	60.05	5.44	11.27	25.64
100	88.06	60.27	5.51	11.51	26.43
150	88.01	60.24	5.56	11.77	26.67
200	86.97	58.44	5.55	11.82	25.23
250	87.49	60.38	5.42	11.32	26.01
$\alpha$					
0.2	87.76	60.56	5.42	11.41	25.56
0.4	87.46	60.46	5.79	11.49	25.97
0.6	86.97	58.44	5.55	11.82	25.23
0.8	87.74	60.62	5.28	11.49	26.41
1.0	87.90	60.43	5.33	11.28	26.49
$\beta$					
0	87.93	62.27	5.77	10.63	25.60
0.25	87.74	60.14	5.57	11.54	25.85
0.50	86.97	58.44	5.55	11.82	25.23
0.75	87.44	59.79	5.72	11.55	26.83
1.0	87.27	61.63	5.73	11.06	25.86

Table 29. Full general-domain results (Part 4/4) of the analysis on evaluation set size,  $\alpha$ , and  $\beta$ .

Model	Diabetic	PCAM	LC25000	Pollen	Amyloid CAA	Amyloid Diffuse	BloodMNIST	ChestMNIST
<i>All</i>								
Dot	71.67	57.20	39.89	23.51	72.64	18.34	16.87	5.50
TracIn	65.40	56.75	40.03	26.34	90.73	12.84	16.69	3.69
TRAK	43.23	59.23	39.57	12.88	77.16	14.74	25.93	3.60
<b>CHIPS (ours)</b>	68.35	63.66	40.51	25.96	88.06	12.38	21.43	6.24
<i>Logit-only</i>								
Dot	62.45	59.27	31.28	25.96	13.48	63.18	20.90	9.60
TracIn	58.24	61.00	33.89	16.09	8.30	71.48	19.38	10.15
TRAK	64.29	62.24	35.12	26.02	14.73	59.51	17.36	11.74
<b>CHIPS (ours)</b>	59.94	61.30	35.36	20.93	13.72	70.29	17.89	21.50
<i>Visual-only</i>								
Dot	61.96	56.15	37.71	23.00	13.33	47.26	20.05	6.74
TracIn	59.11	53.51	34.99	18.16	28.44	31.75	18.15	13.78
TRAK	71.23	59.48	44.83	32.75	23.59	24.27	15.02	15.37
<b>CHIPS (ours)</b>	64.01	57.61	41.25	42.61	33.29	53.67	20.93	5.48
<i>Text-only</i>								
Dot	71.29	61.81	40.77	24.07	40.91	12.56	17.10	20.57
TracIn	61.86	60.90	39.23	25.71	77.58	13.00	18.65	11.51
TRAK	51.61	57.08	39.55	21.36	34.21	46.31	20.61	11.22
<b>CHIPS (ours)</b>	69.76	60.02	46.83	35.80	25.76	55.13	18.65	12.80

Table 30. Full medical-domain results (Part 1/2) of the analysis on end-point subspace.

Model	ChestXray14	Derma	Oct	OrganA	OrganC	OrganS	Path	Retina	Tissue
<i>All</i>									
Dot	6.17	12.17	20.60	9.48	10.36	11.19	25.42	33.75	4.16
TracIn	6.53	12.02	18.00	13.98	12.85	15.28	22.98	40.50	4.96
TRAK	25.84	12.17	20.90	10.74	10.43	11.22	28.68	26.75	4.46
<b>CHIPS (ours)</b>	16.63	11.87	18.20	12.03	9.64	10.71	23.90	30.25	5.29
<i>Logit-only</i>									
Dot	9.63	11.72	24.10	9.22	9.10	7.31	13.89	21.50	6.13
TracIn	10.82	11.77	22.40	10.54	8.82	7.50	15.08	22.25	5.21
TRAK	6.84	11.92	22.80	9.20	7.80	7.34	15.10	23.25	5.53
<b>CHIPS (ours)</b>	9.49	12.02	22.50	9.42	8.68	7.68	16.18	19.00	5.16
<i>Visual-only</i>									
Dot	3.66	11.62	21.30	11.04	9.30	10.72	24.21	22.75	4.72
TracIn	6.45	10.97	19.80	11.80	12.04	13.90	24.25	26.00	4.95
TRAK	6.20	11.77	18.90	11.51	9.90	10.42	17.19	40.00	5.56
<b>CHIPS (ours)</b>	19.32	12.02	19.60	10.91	10.69	12.22	23.69	26.50	5.31
<i>Text-only</i>									
Dot	11.54	11.97	22.50	11.72	11.81	12.30	23.79	33.00	4.55
TracIn	10.52	12.07	19.80	10.27	12.34	13.11	23.97	40.25	4.69
TRAK	18.09	12.27	22.30	12.52	11.82	12.82	25.97	27.25	6.31
<b>CHIPS (ours)</b>	19.51	11.42	19.70	10.09	9.31	9.67	17.66	39.25	5.09

Table 31. Full medical-domain results (Part 2/2) of the analysis on end-point subspace.

Model	Diabetic	PCAM	LC25000	Pollen	Amyloid CAA	Amyloid Diffuse	BloodMNIST	ChestMNIST
<i>CountSketch</i>								
2k	65.13	59.60	48.05	21.43	35.20	32.39	16.69	4.16
4k	68.35	63.66	40.51	25.96	88.06	12.38	21.43	6.24
8k	63.37	57.97	39.76	17.03	73.36	14.87	22.45	2.14
16k	62.10	55.73	40.00	21.50	79.72	23.67	22.27	3.38
<i>Sparse</i>								
2k	66.86	61.11	40.91	25.27	18.14	68.09	17.45	5.81
4k	68.68	60.15	44.19	23.76	23.67	39.46	10.38	5.01
8k	65.29	65.76	43.33	27.03	41.30	12.49	14.53	4.12
16k	68.51	62.10	43.89	35.89	43.41	56.96	24.26	8.14
<i>SRHT</i>								
2k	32.69	60.39	47.09	33.19	68.64	39.88	18.91	6.90
4k	69.35	58.69	39.04	14.39	88.25	15.72	18.65	8.84
8k	41.47	56.59	39.31	27.66	88.67	20.62	14.21	1.82
16k	65.89	58.36	40.35	41.04	32.65	44.25	12.72	3.77

Table 32. Full medical-domain results (Part 1/2) of the analysis on JL random projection.

Model	ChestXray14	Derma	Oct	OrganA	OrganC	OrganS	Path	Retina	Tissue
<i>CountSketch</i>									
2k	10.10	11.32	17.80	14.33	15.17	16.28	21.18	28.00	5.63
4k	16.63	11.87	18.20	12.03	9.64	10.71	23.90	30.25	5.29
8k	21.02	12.77	17.40	14.20	14.00	13.61	27.45	30.50	5.88
16k	20.71	12.37	21.40	14.04	14.62	13.73	25.96	36.00	8.09
<i>Sparse</i>									
2k	11.39	11.12	23.90	14.60	13.47	13.90	26.13	35.75	6.81
4k	10.47	11.72	20.60	10.70	11.31	11.35	24.35	30.00	6.68
8k	7.93	12.17	15.10	11.33	12.20	15.33	23.16	24.50	5.33
16k	7.06	11.42	20.70	12.30	12.07	12.35	28.83	31.75	5.60
<i>SRHT</i>									
2k	13.51	11.57	22.50	10.75	10.47	10.39	23.23	27.00	5.27
4k	9.45	12.02	17.10	9.60	10.72	11.03	31.63	36.00	6.47
8k	22.18	11.87	17.40	13.21	13.21	13.23	28.70	27.00	5.91
16k	7.81	11.22	18.30	12.30	12.48	11.63	24.75	26.25	6.55

Table 33. Full medical-domain results (Part 2/2) of the analysis on JL random projection.

Model	Diabetic	PCAM	LC25000	Pollen	Amyloid CAA	Amyloid Diffuse	BloodMNIST	ChestMNIST
<i>B32-400M</i>								
Random 10%	63.65	50.20	32.51	72.91	97.26	12.82	14.88	6.86
Random 50%	34.53	52.70	25.68	72.91	97.76	12.50	9.97	28.41
<i>B32-CC</i>								
Random 10%	3.45	63.08	8.80	11.00	1.84	87.94	29.49	2.75
Random 50%	3.11	56.25	23.89	51.85	2.86	87.94	21.60	17.87
<i>B16-400M</i>								
Random 10%	10.74	56.77	39.28	7.23	88.27	59.82	14.44	9.08
Random 50%	17.08	66.73	32.91	8.30	96.46	14.03	7.28	1.24
<i>B16-CC</i>								
Random 10%	46.68	50.49	6.40	21.06	60.28	87.95	6.58	1.56
Random 50%	22.16	50.83	17.95	61.28	62.36	87.95	8.21	1.07

Table 34. Medical-domain results (Part 1/2) of MedTrinity [56] dataset.

Model	ChestXray14	Derma	Oct	OrganA	OrganC	OrganS	Path	Retina	Tissue
<i>B32-400M</i>									
Random 10%	6.05	13.97	25.00	10.77	6.86	5.30	34.50	9.75	5.31
Random 50%	11.29	11.32	22.60	10.68	6.69	6.30	35.72	8.50	5.02
<i>B32-CC</i>									
Random 10%	4.42	9.63	25.00	16.22	8.98	6.24	31.91	14.25	9.18
Random 50%	7.56	11.07	25.00	21.59	14.56	14.72	46.03	16.00	8.01
<i>B16-400M</i>									
Random 10%	4.78	10.62	12.40	13.98	8.57	7.73	27.73	12.75	9.46
Random 50%	2.86	10.62	16.20	13.17	11.93	10.32	30.28	7.50	9.70
<i>B16-CC</i>									
Random 10%	9.89	10.62	25.90	13.04	12.71	13.33	35.65	5.00	6.15
Random 50%	6.45	18.50	25.40	19.92	14.79	15.54	42.45	5.75	4.92

Table 35. Medical-domain results (Part 2/2) of MedTrinity [56] dataset.